DTIC
ELECTE
MAY 23 1992
S    D
C

# COLLEGE
OF
# ENGINEERING

DESCRIPTION OF A 1000 SENSOR CONSTANT
CURRENT ANEMOMETER SYSTEM FOR LOCATING
THREE-DIMENSIONAL TURBULENT BOUNDARY
LAYER SEPARATIONS

by

R. L. Simpson, D.A. Walker, and K.A. Shinpaugh
Department of Aerospace and Ocean Engineering
Virginia Polytechnic Institute and
State University

Report VPI-AOE-185

December 1991

# VIRGINIA
# POLYTECHNIC
# INSTITUTE AND
# STATE
# UNIVERSITY

BLACKSBURG,
INIA

92 5 26 102        )26          92-13893
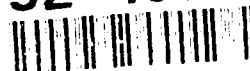
# TABLE OF CONTENTS

# ABSTRACT

The location of three-dimensional separation on bodies such as submarines is important diagnostic information. Considerable changes in the side forces and moments occur with the undesirable phenomenon of separation. Three-dimensional flow separations occur very close to local minima in the magnitude of the wall shear stress. A 1000-flush-surface-sensor constant-current-anemometer separation location system is described here for locating these local minima along the axis of a body.

As shown here, the convective heat transfer coefficient from a sensor is proportional to the one-third power of the local skin friction magnitude for the directionally-insensitive sensors described here. The constant-current anemometer design permits the use of strips of serially-connected sensors that require only one current source per strip. These compact electronics can be housed inside the body.

The voltage drop across each sensor is measured for a number of different computer-controlled currents and related to the local heat transfer coefficient and the fixed parameters for that sensor. Each sensor mounted on the body forms a first order dynamic thermal system whose time constants can be experimentally determined. Thereafter, such as in transient flow separation conditions, measurements only for one current are necessary for a given pre-calibrated sensor.

Results are presented for two sets of tests: (1) flow in the VPI&SU Water Tunnel over a 20° angle-of-attack circular cylinder and (2) a 6:1 prolate spheroid at 15° angle of attack towed in the David Taylor Research Center 140' Basin. The separation location results are in close agreement with those from earlier wind tunnel tests by other investigators.

i

## I. Introduction

In general, premature flow separation is an unwanted phenomenon because it leads to less than ideal performance of a flow machine. In the case of a submarine, crossflow separations form on the leeside of the stern during a turning manuever. Large streamwise vortex structures that contain much circulation are a result, causing a considerable change of the side force and the vertical turning moment of the submarine. The behavior during dynamically unsteady manuevers is even more complicated because of the time-dependent locations of the separations and strengths of the shed vortex structures.

By "separation", we mean the entire process of "departure" or "breakaway", or the breakdown of the boundary-layer flow concept. An abrupt thickening of the rotational-flow region next to a wall and significant values of the normal-to-wall velocity component must accompany breakaway, or otherwise this region would not have any significant interaction with the free-stream flow. In three-dimensional separations the rotational viscous layer can depart from the wall without the surface shear stress necessarily falling to zero, such as occurs in two-dimensional separations. In three-dimensional separations the wall shear stress is zero only at the singular points (Simpson, 1985).

Figure 1 shows a three-dimensional open separation with several characteristic features. Limiting streamlines rising on either side of the line of separation are prevented from crossing by the presence of a stream surface stemming from the line of separation itself. The surface skin friction lines on each side of a separation line converge toward one another, indicating that the low-velocity near wall viscous flow on each side of a separation line accumulates along that line before moving away from the wall. There is no flow reversal along the separation line. The skin friction does not approach zero, although it reaches a local minimum where the lowest velocity near wall fluid is located (Tobak and Peake, 1982). Appendix A is a more detailed discussion of the relationships between surface parameters and the separation line location.

Figure 2 shows data from wind tunnel tests of a 6:1 prolate spheroid that indicate two separation locations, S1 and S2, approximately where local minima of the skin friction magnitude occur. Note that the skin friction lines converge to the separation line from either side, as previously discussed above. Therefore, a technique which is to experimentally locate three-dimensional separation should either find the location of the minimum surface shear stress magnitude as discussed in Appendix A or give the direction of the shear stress lines so that their convergence can be identified.

Moskovitz and Simpson (1990) investigated several schemes for detecting one of these two features. Since the locations of the separations change with angle of crossflow, speed of the submarine, and the unsteady effects of a particular manuever, a separation location system should have sufficient transient response to capture the changing locations of separation. They concluded that a series of flush-mounted heated-foil elements was the best approach for locating minima in the skin-friction magnitude in time-dependent water flows.

This report describes some of the effort to date in the development of a constant current anemometer system to determine the locations of three-dimensional crossflow separations on submarines. The following section is an analysis that shows the relationship between forced convection heat transfer and the local mean skin friction. Section III of this report is devoted to natural or free convection heat transfer effects that can become important at sufficiently low flow velocities.

A specially-designed heat transfer element that is insensitive to flow direction is described in section IV, along with data reduction equations and an analysis of the transient response of a sensor.

Section V deals with sensor covering and waterproofing materials.

Section VI describes the electronics that have been designed to accommodate up to 1000 sensors that will be mounted on the stern of the 16' long rotating arm model for use at the David Taylor Research Center. Portions of these electronics were modified in order to conduct the tests in the VPI&SU Water Tunnel and in the DTRC 140' Carriage Basin that are described here.

Section VII describes the experimental results of tests performed in the VPI&SU Water Tunnel. A series of tests was conducted on three-dimensional flow over a circular cylinder at 22 degrees angle of attack to the flow. Section VIII describes a series of tests conducted at the David Taylor Research Center on three-dimensional flow over a 6:1 prolate spheroid at 15° angle of attack. These tests show that data from this constant-current anemometer system locate the of 3-D separations.

## II. <u>Analysis of Forced Convection from a Single Heated Sensor to a High Prandtl Number Fluid</u>

For a small surface area constant current anemometer sensor used in water, we can employ a high Prandtl number analysis that restricts the thermal boundary layer to the viscous sublayer next to the wall. The approach velocity profile is already developed and does not change much over the length of the sensor. Here we wish to obtain the relationship between the mean velocity gradient at the wall and the average heat transfer rate over the sensor.

The thermal energy transport equation near the wall is given by

$$U \, \frac{\partial T}{\partial x} \; = \; \alpha \, \frac{\partial^2 T}{\partial y^2} \tag{1}$$

for locally two-dimensional flow. Since the flow upstream of the sensor is unheated the incoming flow temperature is the same as that of the freestream, $T_\infty$. The thermal boundary layer grows from the upstream edge of the sensor, but remains entirely within the near wall region if the sensor is short enough in the streamwise direction. We make that assumption

2

here which justifies the use of the following near wall velocity profile

$$U = \left.\frac{\partial U}{\partial y}\right)_w y \tag{2}$$

where $\partial U/\partial y)_w$ is the mean velocity gradient at the wall. The surface shear stress $\tau_w$ is given by $\tau_w = \mu(\partial U/\partial y)_w$.

Substituting the non-dimensional temperature

$$\mathbf{T} = \frac{T - T_w}{T_\infty - T_w} \tag{3}$$

into equation (1) and using (2) produces

$$\left.\frac{\partial U}{\partial y}\right)_w y \frac{\partial \mathbf{T}}{\partial x} = \alpha \frac{\partial^2 \mathbf{T}}{\partial y^2} \tag{4}$$

The boundary conditions on the fluid for this problem are

$$\mathbf{T} = 0 \quad \text{at} \quad y = 0 \tag{5a}$$

$$\mathbf{T} = 1 \quad \text{as} \quad y \to \infty \tag{5b}$$

$$\mathbf{T} = 1 \quad \text{at} \quad x = 0 \tag{5c}$$

A dimensionless similarity variable $\eta$ can be found that reduces equation (4) to a linear ordinary differential equation

$$\eta = \frac{y(\partial U/\partial y)_w^{1/3}}{(3\alpha x)^{1/3}} \tag{6}$$

$$\mathbf{T}'' + \eta^2 \mathbf{T}' = 0 \tag{7}$$

Using equation (6) the boundary conditions then become

$$\mathbf{T} = 0 \quad \text{at} \quad \eta = 0 \tag{8a}$$

$$\mathbf{T} = 1 \quad \text{as} \quad \eta \to \infty \tag{8b}$$

The solution to equation (7) using boundary conditions (8) is

$$\mathbf{T} = M \int_o^\eta e^{-\eta^3/3} d\eta \tag{9}$$

where

$$1/M = \int_o^\infty e^{-\eta^3/3} d\eta = \frac{1}{3}\Gamma\left(\frac{1}{3}\right) = 0.893 \tag{10}$$

3

The heat flux at the surface is given by

$$\dot{q}''_w = -k \left.\frac{\partial T}{\partial y}\right)_w = -k(T_\infty - T_w) \left.\frac{\partial \mathbf{T}}{\partial y}\right)_w \tag{11}$$

which becomes

$$\dot{q}''_w = Mk(T_w - T_\infty)\frac{(\partial U/\partial y)_w^{1/3}}{(3\alpha x)^{1/3}} \tag{12}$$

using equation (9).

For a rectangular sensor of constant width $w$ in the spanwise direction, we can obtain an average heat transfer rate over its length $\ell$

$$\dot{\bar{q}}_w = w\int_o^\ell \dot{q}''_w dx = \frac{3}{2}Mkw(T_w - T_\infty)\frac{(\partial U/\partial y)_w^{1/3}}{(3\alpha)^{1/3}}\ell^{2/3} \tag{13}$$

which means that the average convective conductance is

$$\bar{h} = \frac{\dot{\bar{q}}}{\ell w(T_w - T_\infty)} = \frac{3}{2}Mk\frac{(\partial U/\partial y)_w^{1/3}}{(3\alpha\ell)^{1/3}} \tag{14}$$

Note that the measured $\bar{h}$ is directly proportional to $(\partial U/\partial y)^{1/3}$ and all other parameters in this equation are properties of the fluid and the sensor.

Thus, if the sensor is sensitive only to the magnitude of the wall shear stress, as in the present design, measurements of $\bar{h}$ from a row of nearby sensors permit the location of local minima in $\bar{h}$ and $(\partial U/\partial y)_w$. Here we calculate $\dot{\bar{q}}$ and $(T_w - T_\infty)$ directly from electrical measurements of the sensor condition, as described in the section below on the sensor design and behavior.

## III. Consideration of the Nature of Combined Forced and Free Convection Heat Transfer

The analysis in the last section assumed that free-convection-induced heat transfer was negligible. Clearly this is not always the case, especially near stagnation points and zones of two-dimensional separation where there is flow reversal. In this section an integral analysis of combined forced and free convection will be presented that will allow us to assess the relative effects of free convection for three-dimensional separations.

The governing thermal energy equation in the fluid is

$$U\frac{\partial T}{\partial x} + V\frac{\partial T}{\partial y} + W\frac{\partial T}{\partial z} = \alpha\frac{\partial^2 T}{\partial y^2} \tag{15}$$

We will allow forced convection in the $x$ direction and the positive $z$ direction opposite to the gravitational acceleration vector $\vec{g}$. As in the last section, we will assume that equation

4

(2) holds and $V \approx 0$ near the wall. We will utilize the commonly used free-convection-induced velocity profile (Holman, 1990)

$$\frac{W}{G} = \frac{y}{\delta_T}\left(1 - \frac{y}{\delta_T}\right)^2 \tag{16}$$

where

$$G = \beta\frac{\delta_T^2 g\ (T_w - T_\infty)}{4\nu} \tag{17}$$

Here $\beta = -\frac{1}{\rho}\frac{\partial\rho}{\partial T}$, $\delta_T$ is the local thermal boundary layer thickness, and $\nu$ is the kinematic viscosity. Equation (16) satisfies the exact boundary condition for $\partial^2 W/\partial y^2$ at the wall from the $z$ direction momentum equation, the no slip condition $W = 0$ at $y = 0$, and the artificial condition $\partial W/\partial y = 0$ at $y = \delta_T$.

We will use the temperature profile

$$\frac{T - T_\infty}{T_w - T_\infty} = \left(1 - \frac{y}{\delta_T}\right)^2 \tag{18}$$

which satisfies the conditions: $T = T_w$ at $y = 0$; and $T = T_\infty$ and $\partial T/\partial y = 0$ at $y = \delta_T$.

Substituting all of these relations into equation (15) and integrating with respect to $y$ produces

$$\rho c_\rho\frac{\partial U}{\partial y}(T_w - T_\infty)\delta_T^2\ \frac{\partial}{\partial x}\left[\int_o^1\left(1 - \frac{y}{\delta_T}\right)^2\frac{y}{\delta_T}\ d\left(\frac{y}{\delta_T}\right)\right]$$

$$+\rho\ c_\rho\ G\ \delta_T^2(T_w - T_\infty)^2\frac{\partial}{\partial z}\left[\int_o^1\left(1 - \frac{y}{\delta_t}\right)^4\frac{y}{\delta_T}\ d\left(\frac{y}{\delta_T}\right)\right]$$

$$= 2k\ \frac{(T_w - T_\infty)}{\delta_T} = \dot{q}_w'' \tag{19}$$

for a constant surface temperature sensor. This further becomes

$$\frac{7}{12}\ \frac{\partial U}{\partial y}\ \frac{\partial}{\partial x}(\delta_T^2) + \frac{\beta\ g(T_w - T_\infty)}{120\ \nu}\ \frac{\partial}{\partial z}(\delta_T^3) = \frac{2\alpha}{\delta_T} \tag{20}$$

After further rearranging, this equation becomes

$$\frac{7}{36}\ \frac{\rho c_\rho}{k}\ \frac{\partial U}{\partial y}\ \frac{\partial\delta_T^3}{\partial x} + \frac{\rho\ \beta\ c_\rho\ g}{240\ \nu\ k}\ (T_w - T_\infty)\delta_T\ \frac{\partial\delta_T^3}{\partial z} = 1 \tag{21}$$

The initial conditions for this non-linear differential equation for a rectangular sensor of length $\ell$ and width $w$ are $\delta_T = 0$ along $x = 0$ and $\delta_T = 0$ along $z = 0$. The latter

5

condition is not exactly rigorous because $W$ is not zero along $z = 0$ because of continuity requirements on the free-convection-induced flow.

Integrating equation (20) over the area of a sensor produces an equation for the total heat transfer rate

$$\frac{7\rho c_p}{12}(T_W - T_\infty)\frac{\partial U}{\partial y}\left[\int_o^W \delta_T{}^2 dz\right]_{x=\ell} + \frac{\rho\,\beta\,c_p\,g(T_w - T_\infty)^2}{120\,\nu}\left[\int_o^\ell \delta_T{}^3 dx\right]_{z=w} = \dot{q} \quad (22)$$

with the first term representing the forced convection heat transfer and the second term the free convection.

The property groupings for these two terms produce insights on the relative magnitude and temperature dependence of forced and free convection. Over the range of 16°C to 38°C, where we expect to operate, $\rho$ and $c_p$ for water are constant within $\pm 1/4\%$ while $k$ increases less than 8%. Thus the thermal properties grouping associated with the forced convection term of equation (21) decreases about 8% from 10°C to 38°C. The free convection grouping $\rho\,\beta\,c_p\,g\,/\,k\,\nu$ varies almost linearly with temperature and <u>increases</u> by a factor of about 5.2 over this temperature range. Thus, the coefficient of the second term of equation (22) varies with about $(T_w - T_\infty)^3$ while the forced convection term coefficient varies with about $(T_w - T_\infty)$.

The closed form solution of equation (21) is implicit in terms of $\delta_T$ and is not readily available to substitute into equation (22). Since we wish to obtain the forced convection contribution to equation (22), we can develop an experimental procedure using data at various $(T_w - T_\infty)$ and the form of equation (22)

Equation (22) can be written in the form

$$F_1\,(T_w - T_\infty) + F_2\,(T_w - T_\infty)^2 = \dot{q} \quad (23)$$

$F_1$ is the forced convection term coefficient that varies principally with $\partial U/\partial y$ since the properties do not vary much with temperature and the geometry of a given sensor is fixed. $F_2$ is a function associated with the free-convection and depends on the fluid properties, sensor geometry, and sensor operation. It increases significantly with the average temperature $T_m = (T_w + T_\infty)/2$, which is used to evaluate properties. $F_1$ is the slope of a plot of $\dot{q}$ vs. $(T_w - T_\infty)$ as $(T_w - T_\infty) \to 0$, as shown in equation (23).

In order to estimate when free convection effects may be significant, we can look at the ratio of the free convection term to forced convection term in equation (21). The dimensionless ratio of the coefficients to the derivatives is

$$R = \left(\frac{\rho\,\beta\,c_p\,g\,(T_w - T_\infty)\delta_T}{240\,\nu\,k}\right) / \left(\frac{7}{36}\,\frac{\rho c_p}{k}\,\frac{\partial U}{\partial y}\right) \quad (24)$$

This indicates that free convection is small when $\delta_T$ is small in the presence of any forced convection. We can estimate $\delta_T$ from the pure forced convection solution given in the last section.

6

Forced convection $\delta_T = \dfrac{2}{M} \dfrac{(3\,\alpha\,\ell)^{1/3}}{(\partial U/\partial y)^{1/3}}$ (25)

Thus

$$R = 0.0556 \left( \frac{\rho\,\beta\,c_p\,g}{\nu\,k}(T_w - T_\infty)\alpha^{4/3}\ell^{1/3} \right) / (\partial U/\partial y)^{4/3}$$ (26)

This indicates that we can minimize free convection effects by using low $(T_w - T_\infty)$ and short sensors ($\ell$ is small).

Consider water at the average properties temperature of about 21°C, then equation (26) produces

$$R = \left( \frac{0.63}{m^{1/3}\,°C\ sec^{4/3}} \right) \frac{(T_w - T_\infty)\ell^{1/3}}{(\partial U/\partial y)^{4/3}}$$ (27)

For $R < 0.1$, then this indicates that

$$\frac{\partial U}{\partial y} > \frac{3.98}{m^{1/4}\,°C^{3/4}}(T_w - T_\infty)^{3/4}\ \ell^{1/4}$$ (28)

As long as this criterion is met, free convection effects should be less than about 10% of the total heat transfer.

## IV  Sensor Design and Behavior

Figures 3 and 4 show two designs of nominally directionally insensitive constant current anemometer sensor foil. The sensor shown in Figure 3 have a ± 6% variation of heat transfer with direction, while the second design has a ± 1% variation. These variations were determined for various orientations of a sensor by assuming that the convective heat transfer from a given length of the sensor element varied with the cosine of the angle of the flow from the normal to the element; the contributions from each element were then summed.

The sensor foil of thickness $t$ is mounted on a substrate material of thickness $t_s$ and covered with a material of thickness $t_c$, and has a planform surface area $A_s$. A layer of adhesive of thickness $t_a$ is between each of the other layers. Thus, a sensor is a five layer sandwich as shown in Figure 5. When applied to the surface of a model, an additional layer of adhesive $t_a$ must be used. For the MINCO sensors shown in Figure 3, $t_c = t_s = t_a = 0.0005$ inches and $t = 0.0002$ inches. The cover and substrate materials are kapton and the foil is Balco (70% nickel, 30% iron) with the temperature coefficient of resistivity $\alpha = 0.0051/C°$. Table 1 is a list of properties of materials.

Sensors are manufactured in rows with interconnecting leads as shown in Figure 6. A constant current $I$ from a single source is passed through the entire row of sensors. The Joule heating in each sensor $I^2R$ is convected away by the fluid. Ideally, we would prefer no conduction into the substrate and model and no thermal resistance to heat transfer into the water.

7

In steady state, the Joule heating equals the heat transfer into the substrate and model and the heat transfer into the water

$$\dot{q} = I^2 R = I^2 R_\infty [1 + \alpha (T_f - T_\infty)] = (T_f - T_\infty)(\pi_1 + \pi_2) \tag{29}$$

where $T_f$ and $T_\infty$ are the temperatures of the foil and water, respectively.

Here,

$$\pi_1 = \frac{A_s}{\left( \frac{t_c}{k_c} + \frac{t_a}{k_a} + \frac{1}{h} \right)} \tag{30}$$

is the thermal conductance into the water and

$$\pi_2 = \frac{A_s}{\left( \frac{t_s}{k_s} + \frac{2t_a}{k_a} + \frac{t_m}{k_m} \right)} \tag{31}$$

is the conductance into the model of wall thickness $t_m$ and thermal conductivity $k_m$. For a fiberglass model wall of the order of 1/4 inches thick, $\pi_2 \approx \pi_1 \times 10^{-2}$, and the heat transfer is mainly into the water. Ideally, the thermal resistance of the cover and adhesive material $(t_c/k_c + t_a/k_a)$ should be made close to zero.

Equation (29) can be rearranged to give

$$(T_f - T_\infty) = \frac{I^2 R_\infty}{(\pi_1 + \pi_2 - \alpha I^2 R_\infty)} \tag{32}$$

Because $R$ varies with $\alpha$ and $(T_f - T_\infty)$ as implied in equation (29), the steady state voltage drop across a sensor is

$$V = I R_\infty [1 + \alpha (T_f - T_\infty)] \tag{33}$$

Equations (32) and (33) can be combined and the voltage sensitivity to $h$ calculated

$$\frac{\partial V}{\partial h} = \left( \frac{\partial V}{\partial \pi_1} \right) \left( \frac{\partial \pi_1}{\partial h} \right) = \frac{-\alpha I^3 R_\infty^2 \pi_1^2}{A_s (\pi_1 + \pi_2 - \alpha I^2 R_\infty)^2 h^2} \tag{34}$$

In the limit of $\pi_2 \rightarrow 0$ (no heat transfer to the substrate) and $\pi_1 \rightarrow h A_S$ (no cover and adhesive thermal resistance), equation (34) becomes

$$\frac{\partial V}{\partial h} = \frac{-\alpha I^3 R_\infty^2 A_S}{(h A_S - \alpha I^2 R_\infty)^2} \tag{35}$$

In both equations (34) and (35), we see that the sensitivity of the voltage with respect to the convective conductance $h$ varies stronger than the individual variations of $\alpha$, $I^3$, $R_\infty^2$, $1/h^2$, and $1/A_S$. Equation (35) is an important design equation, indicating that we should minimize heat transfer to the substrate and model, reduce thermal resistance of the covering materials within waterproofing constraints, select a high $\alpha$ foil material, minimize $A_s$

8

within manufacturing constraints, and maximize $I$ and $R_\infty$ within maximum voltage drop and manufacturing constraints.

In practice we measure the cold resistance $R_\infty$ of each sensor, the voltage $V$ across each sensor, and the current $I$ which is held constant. Thus we can calculate the foil temperature difference

$$T_f - T_\infty = \frac{1}{\alpha}\left(\frac{V}{IR_\infty} - 1\right) \tag{36}$$

and the heat transfer rate

$$\dot{q} = VI \tag{37}$$

Using the defining equation for $h$

$$\dot{q} = h\,A_s(T_w - T_\infty) \tag{38}$$

in terms of the sensor cover outer temperature, assuming that all of the heat transfer is into the water, and using the thermal resistance ratio

$$\frac{T_w - T_\infty}{T_f - T_\infty} = \frac{1}{h\left(\frac{t_c}{k_c} + \frac{t_a}{k_a}\right) + 1} \tag{39}$$

we can calculate the surface temperature difference

$$T_w - T_\infty = (T_f - T_\infty) - \frac{\dot{q}}{A_s}\left(\frac{t_c}{k_c} + \frac{t_a}{k_a}\right) \tag{40}$$

Note that $\dot{q}$ and $(T_f - T_\infty)$ are derived from experimentally measured quantities and equations (36) and (37) and the other quantities are properties of the sensor and the covering materials. Finally, equation (38) can be used to determine $h$.

To examine the transient response of a sensor, we can consider a time-dependent contribution to the convective conductance, $h(\tau)$, which forces a transient temperature difference $\theta(\tau)$ of the foil. The governing linearized first term unsteady heat transfer equation is

$$M\,\frac{d\theta}{d\tau} = -[\pi_1 + \pi_2 - \alpha I^2 R_\infty]\theta - \frac{(T_f - T_\infty)\pi_1^2 h_1(\tau)}{A_s h^2} \tag{41a}$$

or

$$M\,d\theta/d\tau = -N\,\theta - P\,h_1(\tau) \tag{41b}$$

where $\pi_1$, $\pi_2$, $(T_f - T_\infty)$, and $h$ are from the steady state mean flow case described above, and

$$M = A_S \sum_i (\rho_i\,c_{pi}\,t_i\,B_i) \tag{42}$$

is the sum of the lumped parameter thermal capacitance for each layer $i$ of the sensor sandwich. Here $B_i$ is the steady state ratio of $(T_i - T_\infty)/(T_f - T_\infty)$ for each layer of the sandwich.

For a sinusoidal variation of $h_1(\tau)$

$$h_1(\tau) = h' \sin(\omega\tau) \tag{43}$$

the solution of equation (41) is

$$\theta(\tau) = \frac{-\omega P h'}{M(\omega^2 + N^2/M^2)} \left\{ \frac{N}{\omega M} \sin(\omega\tau) - \cos(\omega\tau) + e^{-\frac{N}{M}\tau} \right\} \tag{44}$$

for $\theta = 0$ at $\tau = 0$. For large time $\tau$

$$\theta(\tau) = \frac{P\,h'\,\sin(\omega\tau + \phi)}{M(\omega^2 + N^2/M^2)^{1/2}} \tag{45}$$

where

$$\phi = \pi + \tan^{-1}\left( -\frac{\omega M}{N} \right) \tag{46}$$

is phase shift. Note that as $M \to 0$, $\theta$ is 180° out of phase with $h_1$. The voltage variation across the sensor is

$$V(\tau) = \alpha I R_\infty \theta(\tau) \tag{47}$$

For a ramp variation of $h_1(\tau)$

$$H_1(\tau) = (dh/d\tau)_1 \tau \tag{48}$$

the solution of equation (41) with $\theta = 0$ at $\tau = 0$ is

$$\theta(\tau) = -P\left(\frac{dh}{d\tau}\right)_1 \left\{ \frac{\tau}{N} - \frac{M}{N_2} + \frac{M}{N_2} e^{-\frac{N}{M}\tau} \right\} \tag{49}$$

For large time $\tau$, the time delay $D$ is found by equating $\theta(\tau)$ for $M = 0$ to $\theta(\tau + D)$ for $M \neq 0$:

$$\theta(\tau)/M=0 = -P\left(\frac{dh}{d\tau}\right)_1 \frac{\tau}{N} = -\frac{P}{N}\left(\frac{dh}{d\tau}\right)_1 \left(\tau + D - \frac{M}{N}\right) \tag{50}$$

Thus, the time delay

$$D = M/N \tag{51}$$

which indicates that piecewise continuous ramp variations of $h_1(\tau)$ result in a time delay response that is independent of the ramp slope $(dh_1/d\tau)$.

## V Sensor Covering and Waterproofing Materials

The analysis in section IV describes the need for a thin coating with high thermal conductivity to give the sensor the highest sensitivity obtainable for a given design. The coating used and its application are of primary concern to the success of the system. For

this reason it has been decided to manufacture future sensor strips without a cover, since the thinnest kapton or upilex covers available are 0.5 mils with a thermal conductivity $k$ no better than 1.4 BTU-in/(R-hrft$^2$), such as used in the tests reported here. Removal of the cover also eliminates a layer of adhesive (on the order of 0.5-1.0 mils with a conductivity of 1.3 BTU-in/(R-hr-ft$^2$)). In the future, strips should be covered in situ with a constant thickness layer of high thermal conductivity epoxy that will also water proof the sensors, as discussed below.

The requirements of the coating and/or coatings upon the sensing surfaces are severe. The coating must have a high dielectric strength, a low dielectric constant and a low rate of water absorption as well as a high thermal conductivity. The required shear strength will be relatively low for an adhesive, thus the coating will only need a nominal value for shear strength. The coating needs to be applied uniformily over the sensor's surface such that directional sensitivity is not induced; furthermore, each individual sensor needs the same coating thickness to maintain relatively uniform sensitivity between sensors. Different coating application methods were investigated with cost, uniformity, repeatability and relative thermal resistance ($t_c/k_c$) being of prime concern.

One option consists of using a drip method using thinned epoxies with high thermal conductivities (Master Bond* Polymer Adhesive EP 21A, 25 BTU-in/(R-hr-ft$^2$)). The sensor strip is mounted vertically with a layer of epoxy applied above the sensing surface. Gravity forces the epoxy over the sensing surface. This method requires the strips to be mounted to the model before the coating is to be applied, which could be a problem due to the geometry constraints. Uniformity could be easily controlled to approximately +/- 20% thickness but a coating of no less than 3 mils could be obtained. The thickness of the coating could be reduced if extreme care was taken but uniformity between sensors and especially between sensor strips would always be suspect. This method should be only used to evaluate different coatings.

In the second method investigated, a highly thinned layer of high thermal conductivity epoxy was sprayed onto the sensing surface with an air brush, specially made to shoot epoxy. It has been shown that the thinnest layer which may be applied is 2 mils. Better uniformity is achieved with this method over the drip method. However, substantial skill would have to be developed. This method also requires the bonding of the strip to the model before the coating application, but does not require the strip to be at a specific orientation. Room conditions would have to be controlled though.

The third and most reliable method produces a constant thickness layer of high $k$ epoxy without special application skills or handling of sensors before their mounting on the model. A strip of thin (2 mils) plastic tape is applied on each side of a row of sensors after they have been mounted on the model. The high $k$ epoxy is applied to the sensors. A teflon spreader is moved across the top of both plastic tape strips, leaving a uniform layer of the epoxy in between. After the epoxy partially sets up, the two tape strips are removed, along with any epoxy remaining on top of those strips.

---

* Master Bond, P.O. Box 522, Teaneck, N.J. 07666.

Another possible covering is a conformal polymer coating. The best conformal coating found for this application has been Parylene, applied by Nova Tran Corp.** which is a subsidiary of Union Carbide Corp. This method will produce uniform coatings which will be consistent among sensor strips since the group of strips which will be used on a given model will be coated at the same time under the same conditions. A coating has been investigated which when applied at a 1 micron thickness will give a breakdown voltage of greater than 500 volts, giving an order of magnitude of margin upon the breakdown voltage. The coating is applied such that no pinholes exist at a 0.1 micron thickness. Furthermore, the water absorption rate is less than 0.1% by mass over a 24-hour period; thus substantial waterproofing should be obtained. The thermal conductivity of the material is only 0.6 BTU-in/(R-hr-ft$^2$); however, due to the thickness of application a reduction of an order of magnitude of effective thermal resistance can be obtained when compared with a sensor strip manufactured with a kapton cover. This covering must be applied at the Nova Trans plant before mounting to the model. The conformal coating is highly flexible and will not hinder the application of the sensor strips to the model. The manufacturer of the coating has suggested a thickness of no less than 1 micron such that the coating will be able to sustain mild abuse. The constant thickness high $k$ epoxy method was still judged superior to paralyne since in situ repairs can be made with the epoxy.

The epoxy used to bond the sensor strips and connectors to the model is Hydrobond 600, which is manufactured by Superior Polymer Products***. The Hydrobond has a water absorption rate of 0.1% by mass over a 24 hour period even when applied underwater. This epoxy is semi-flexible when cured. The user is able to control the pot life and the viscosity by adding and subtracting various components. The hydrobond is also used to coat the connections to the sensor strip since lab tests have shown that it has sufficient electrical strength for applications with sensors underwater. The electrical properties of the connector coating are less stringent than the sensor coating because the thickness of the coating can be much thicker for this application. Additional electrical insulation can be obtained at the connections by using strain gage technology, which incorporates teflon sheets, although we found this to be unnecessary.

## VI  Description of the Constant Current Kilo Anemometer Electronics, Data Acquisition Hardware & Program

Our purpose is to apply flush mounted hot film sensors to the surface of a model to detect the location of the three-dimensional separation lines. Hot-film sensors are a good choice because they are directly sensitive to the local shear stress and relatively easy to manufacture in large arrays. For the application to the 16' rotating arm submarine model, on the order of 1000 sensors are needed to define the position of a separation line with sufficient peripheral spatial resolution.

The most practical way to connect 1000+ constant current hot-film sensors is in series in groups of N sensors, passing a common constant current through all sensors in each

---

** Nova Trans Corp., 100 Deposition Drive, Clear Lake, Wis. 54005.
*** Superior Polymer Products, 1700 Duncan Ave., Hubbell, Mich. 49934.

group. This reduces the number of leads and the number of current sources. The number of leads is thus reduced to N+2 instead of 2N for each group (or sensor string). Practical values of N range from approximately 10 to 60, depending on the sensor size and resistance, the maximum current available, the maximum voltage available, and the fluid and flow properties. Such systems for use in air with up to 96 sensors have been built (Feyzi et al., 1989).

Here, an anemometer system for up to 1024 sensors based on this scheme was designed and built for use in water. The electronics of the system consist of constant current sources, preamplifiers, multiplexers, a computer interface, and a pair of transmission line interfaces. The system was designed to fill a total of ten circuit boards, eight anemometer boards and two interfacing boards. The distribution of the above functional sections on the boards deserves comment. Since multiple printed circuit boards were required, each of the eight main boards was designed to include most of the functions for 128 of the sensors. This not only allowed a variation of the number of sensors by varying the number of boards, but it minimized the number of interboard connections, since these now followed the first stage of 16:1 multiplexers.

The etch patterns for the main printed circuit boards were produced at Virginia Tech. From these the boards were manufactured by Appalachian Electronics. Only one board was needed for the 140 foot towing tank tests and the VPI and SU Water Tunnel tests described below.

A. <u>Constant current sources</u>

The voltage-controlled current sources consist of two stages of op amps with a power FET output capable of producing up to one amp of regulated current at up to 40 v. Each of the eight boards has four current sources (Walker et al., 1992). All of the current sources follow the same calibration curve (within one per cent). Calibration of one of the current sources is shown in Figure 7.

The current is software-controlled via the voltage from a D/A output of the computer. The sensors are not turned on until the model is in motion. The current can then be fixed or stepped through a set of programmed values and returned to zero before the model is brought to rest and the test terminated. The use of multiple currents for each sensor aids the correction for any natural convection by allowing extrapolation to zero current and provides a least squares method for finding the forced convection heat transfer conductance.

Each current source operating from 40 v used in the 140 foot towing tank provided power for up to 14 sensors at 450 ma or 28 sensors at 265 ma with (MINCO) sensors. The sensor design for the rotating arm test will allow 32 sensors per string to carry 375 ma.

B. <u>Anemometer amplifiers</u>

Each anemometer board contains 128 differential amplifiers, consisting of 32 PMI OP400 quad op amps and 72 resistor arrays (Walker et al., 1992). Amplifiers, such as these, are required to eliminate the common-mode voltage resulting from the other sensors in each string. Each amplifier observes the voltage difference across one of the sensors. The amplifiers also provide a modest gain (3-10) to raise the signal levels away from noise and interference.

At very low current settings- used to measure the sensor cold resistances, typically 20 ma- the current load due to the amplifier resistors cannot be neglected. To correct for this an algorithm for individual sensor currents was applied.

## C. Analog multiplexing/ digital control

Each board had eight 16:1 multiplexers (Harris IH6116 for the towing tank, DG506A for the rotating arm system). The outputs of the eight multiplexers from each of the anemometer boards are fed through four more 16:1 multiplexers on a ninth board, which reduces the 1024 total possible sensor signals to four. The four remaining signals are transmitted to the remote computer A/D converter board.

To control which sensor is read, each sensor may be polled independently in any order and at any rate up to the maximum transfer rate by the host computer. Individual sensors are addressed in blocks of four by the computer via an eight bit address, digitally transmitted to the anemometer boards. Each of the four sensors in a block are distinguished by its A/D input channel. For the present application all of the sensors are polled in a fixed sequence.

The maximum rate that the sensor addresses can be sequenced is much higher than the rate that the sensor data can be A/D converted and stored and is therefore not a factor at present.

## D. Analog transmission

The data from the sensors can be sampled with an A/D converter inside a computer at a distance of 250 feet from the submarine model, although in the 140' Basin tests the computer was mounted on the carriage with no more than 20 feet of cable. To transfer data at the required rate and to avoid degradation of the signal due to interference or cable ringing, an analog line driver was designed. The transmission lines will be shielded cables and both ends of the transmission lines are impedance matched. Tests were conducted to verify that the required data transfer rate of 10 samples per second per sensor would be reached. The tests, conducted over both a coaxial cable and shielded twisted pairs nearly 1000 feet long, demonstrated that data rates even higher than the required rate could be achieved over the required transmission distance.

## E. Submersion housing for electronics

For the future rotating arm tests the 1000 anemometer system must reside inside the

flooded marine model. To protect the electronic boards from contact with water or the supporting sting, a plexiglas and rubber housing has been designed, machined and tested for fit in the model. The housing consists of a plexiglas "box" which contains a neoprene liner filled with an insulating gel in which the pc boards are inserted. The gel assures that the pressure inside and outside the bag is the same at any submersion depth and it helps to remove heat from the circuits. The housing is horse-shoe shaped so it can wrap around the sting and to allow its installation from the side of the model while the sting is in place.

## F. Data Acquisition Hardware and Program

Data acquisition was performed on an IBM PS/2 Model 60 with a National Instruments MC-M10-16 data acquisition board. The MC-M10-16 contains a 12 bit analog-to-digital (A/D) converter with 16 analog inputs, two 12 bit digital-to-analog (D/A) converters with voltage outputs, and eight digital I/0 lines. Multi-channel data acquisition can be performed at rates up to 100 KHz. The board uses computer memory as a storage buffer.

The data acquisition program is written in $C$ language to maximize data acquisition rates and computer storage. Four channels on the MC-M10-16 board are used for data acquisition, the eight digital lines are used to control the multiplexing on the kilo-hotwire board, and the voltage output is used to control the current through the sensors. Currently the data acquisition program uses buffered I/O with a maximum data size of 128 Kbytes or 64 K samples of data. The data are stored in binary data files for later processing.

The data reduction program is also written in the $C$ language. The data are averaged for each sensor over the total number of data points taken; Chauvenet's criterion (Holman, 1989) can be used to remove spurious data points. The data are then corrected to take into account the slightly different current in each sensor due to the loading of the resistor arrays and to also correct for the different gains and offsets in each of the amplifiers associated with each sensor. The resulting voltages are converted to sensor foil temperature difference by $(T_f - T_\infty)$ equation (36) and heat transfer rate $\dot{q}$ by equation (37). A least squares fit of $\dot{q}$ vs. $(T_W - T_\infty)$ by a straight line for the several low currents where forced convection is dominant yields a slope that is proportional to the forced convection conductance $h$. (See equations (23) and (38).)

From these results the location of minimum forced convection heat transfer conductance $h$ is located by using a quadratic least squares fit to the $h$ data from 5 adjacent sensors. This locates the minimum skin friction magnitude since $\tau_W = \mu(\partial U/\partial t)_W \sim h^3$ according to equation (14).

## VII.    Experimental Results of the Performance of the Constant Current Anemometer System in Locating Three-Dimensional Separations on a Circular Cylinder at Angle of Attack in the VPI&SU Water Tunnel

A series of tests was conducted in the VPI&SU water tunnel (2' x 2' crossection) to examine the performance of the constant current anemometer (CCA) system for locating 3-D separations. The photographs in Figure 8 show these tests in progress. A 6.625 inches

15

diameter circular plastic pipe was used as the test body at an angle of attack of 22 degrees. Two rows of CCA sensors were mounted around the cylinder, as shown in the photographs. The approach water flow was at 2 feet per second. From the work of Poll (1985), it is clear that we should expect a primary separation near 105 degrees peripheral angle measured from the windward side, with turbulent reattachment near 115 degrees peripheral angle. A second separation, this time turbulent, should occur at some higher peripheral angle somewhere near 125 to 130 degrees.

At the same time, we used "mini-tufts" that were glued directly to the cylinder upstream of the rows of sensors to observe the boundary layer behavior in that vicinity. These "mini-tufts" were fluorescent-dyed 0.001 inches diameter filaments that were glued at one end to the cylinder surface. While not readily seen under visible light, the unsteady motion of these small filaments can be observed with UV illumination. Other researchers (Crowder, 1980) claim that these tufts can follow unsteady motions up to 30 Hz. However, in the tests described here these tufts remained too far away from the wall to detect the convergence of the flow from each side of a 3-D crossflow separation. As shown in these photos for the 0 degrees angle-of-attack case, these mini-tufts move erratically away from the wall of the cylinder and could not pick up the separation.

Figure 9 shows data from 8 adjacent CCA sensors for the heat transfer rate, $\dot{q}$, vs. the sensor cover temperature difference $(T_w - T_\infty)$ for 8 different sensor currents. A straight line closely fits the data for a given sensor, except for very low currents. The slope of a given straight line is proportional to the heat transfer convective conductance, $h$, according to equation (38). The cube of $h$ is proportional to the local magnitude of the surface shearing stress and is less than $\pm 4\%$ uncertain. Estimates of $(\partial U/\partial y)_W$ from equation (14) indicate that free convection effects are negligible since $R$ in equation (27) is much less than 0.1.

Figure 10 shows a plot of the variation of the magnitude of the shearing stress around the circular cylinder at 22 degrees angle of attack. Since the local minimum in the magnitude of the surface shearing stress is the location of a three-dimensional separation, figure 11 shows that one 3-D separation occurs near 105 degrees peripheral angle, reattachment occurs near 115 degrees, and a second separation occurs near 125 degrees. Considering the resolution limits of these tests and the flow blockage effects of the floor and walls of the water tunnel, the agreement with the results of Poll are quite good.

VIII    Experience and Results of the Performance of the Constant Current Anemometer System in Locating Three-Dimensional Separations on a 6:1 Prolate Spheroid at Angle of Attack in the David Taylor Research Center 140' Towing Basin.

A series of tests was conducted in the DTRC 140' Towing Basin (10' wide x 5' water depth x 140' long) to examine the performance of the constant current anemometer (CCA) system for locating 3-D separations on a 6:1 prolate spheroid model. This 54" long model, shown in Figure 11, is a duplicate model of the one used by Ahn and Simpson (1992) in studying the location of three-dimensional separations in the VPI&SU Stability Wind Tunnel. A 2.75" diameter sting was attached inside the model. Figure 12 shows the 1/16"

16

diameter trip wire located at $x/C = 0.2$.

Three rows of CCA MINCO sensors were mounted near the stern of the leeside of the prolate spheroid model at $x/C$ of 0.7, 0.8, and 0.9, as shown in the photograph in Figure 13. Because the spacing between sensors was 1/2", the angular spacing between the center of each sensor was 7.1° at the first location (x/C = 0.7) and 10.0° at the third location (x/C = 0.9). As mentioned above, Hydrobond epoxy was used to mount the sensor strips in place. Conventional plastic electrical tape was strapped tightly around the edges of each strip and around the model, providing enough elasticity to hold the strips in place while curing the epoxy with conventional heat lamps. This epoxy or an additional layer of "5-Minute" epoxy was also used to form a fillet fairing between the model surface and the sensor strip surface. The taut electrical tape provided a smooth external mold for this fillet.

Ribbon cables were soldered to the lead pads and then epoxied to the model surface as shown in Figures 11 and 13, extending toward the leeside in order to minimize interference with the separation processes nearer the windward side. The ribbon cables were then taped to the sting. The sting was then screwed onto the 140' Towing Basin carriage model mount, as shown in Figure 14. All measurements were made with the model at 15° angle of attack to the direction of the carriage motion. The ribbon cable was taped to the sting mount and connected to the constant current source and amplifier board (Figure 15) and computer (Figure 16) on topside of the carriage.

During each run, the carriage was brought from rest to a nearly constant speed before data were acquired. For the 5 fps runs, it took about 4 seconds to reach a constant speed, leaving about 12 seconds for obtaining data before braking of the carriage. For the 7 fps runs, it took about 5 seconds to reach a nearly constant speed with only 3.6 seconds remaining for taking data. Data were obtained over enough constant speed runs for a total record length of at least 12 seconds for each sensor current. No runs were possible at lower speeds because the carriage speed control failed before these data could be obtained.

As in the earlier tests with the circular cylinder, $\dot{q}$ vs. the sensor cover temperature difference $(T_W - T_\infty)$ was obtained for 7 different sensor currents: 5, 200, 300, 350, 400, 450, and 500 milliamperes (ma). A straight line closely fits the data at a given current, except for the lowest current. The slope of a given straight line is proportional to the heat transfer convective conductance, $h$. The cube of $h$ is proportional to the local magnitude of the surface shearing stress and is less than 4% uncertain.

Figures 17-20 show plots of the variation of the magnitude of the shearing stress around the prolate spheroid at two axial locations (x/C = 0.7 and 0.9) for two different carriage speeds. No data were obtained from the middle row of sensors (x/C = 0.8) which showed no sensitivity, even though much work was done trying to find the source of the problem. A "Thompson's Waterseal" coating had been applied previously to the surface of only this row of sensors, leading us to believe that the effective waterproofing of the original Kapton was greatly reduced by this coating.

Since the local minimum in the magnitude of the surface shearing stress is near the location of a three-dimensional separation, Figures 17 and 18 show that two separations were detected on the leeside ($\phi > 90°$) at x/C = 0.7, while an apparent laminar-to-turbulent transition was detected on the windward side. Although Ahn and Simpson (1992) did not report separation locations for the same Reynolds numbers as obtained in the towing basin, Figures 17 and 18 still show good agreement of the two sets of data, considering the limited spatial resolution of the sensors.

Figures 19 and 20 show the results at x/C = 0.9. Since we anticipated leeside separations near 90° from the earlier work of Ahn (Figure 21), we had mounted available sensors (Figure 13) so as to detect the primary separation. However, Figure 19 shows a separation near 110° and an apparent laminar-to-turbulent transition near 50° for the slower case. Figure 20 also shows an apparent laminar-to-turbulent transition near 50° for the higher speed case, but the shear stress magnitude is continuing to decrease at the leeward end of the sensor strip. Figure A.1 in the Appendix (albeit 30° angle of attack data) shows that near the stern of the prolate spheroid, the shear stress magnitude greatly decreases over a relatively small peripheral angle change near the primary separation. This feature is reproduced in Figure 19. Figure A.1 also shows that the shear stress magnitude remains at a relatively low level further around the leeward side of the body.

Nevertheless, at x/C = 0.9 there is not good agreement with Ahn's data. The Reynolds number differences could be part of the reason, although Ahn and Simpson do not show much effect of Reynolds number at the location. The data of Kreplin et al. (1985) for 15° angle of attack at a Reynolds number of 6.53 x $10^6$ using natural transition indicate that shear stress minima occur about 15° further around the body at all x/C locations than the results of Ahn and Simpson.

However, the most likely reason for this apparent discrepancy with the oil flow work of Ahn and Simpson is that the leads and ribbon cable for the last row of sensors were placed on the windward side of the model. Even though the flow passing over these protuberances would not pass over sensors, it could have been affected by them. Also, Ahn and Simpson used a 2" diameter sting through the stern end of their identical model, whereas we used a 2.75" diameter sting in the currently reported tests.

Although all of the above discussed data were obtained after the sensors and the flow speed had reached steady state conditions, the transient responses of these sensors is of much interest because of their intended future use under transient conditions. Tests were conducted to determine the worst case response times of the hot-film sensors. Since the current was computer controlled, it was possible to turn on the current at time zero and then sample the history of the response voltage as the sensors heated up. The results for the MINCO sensors on the prolate spheroid model at zero flow indicate that there are three time constants, 0.01 sec., 0.121 sec., and 4.36 sec., instead of one as modeled in the analysis beginning with equation (41). In other words, there are three exponentially decaying terms instead of just one as given in the analysis. Also found were the weighting functions for these exponentials, 0.905, 0.035, and 0.06, which indicate the fraction of the thermal capacity lag effect in the balco foil, the kapton cover, and the kapton and

18

fiberglass substrate, respectively. Examination of the analysis beginning with equation (41) reveals that the zero flow case is the worst case in regard to the transient response since the governing equations are non-linear. The presence of some mean flow convective heat transfer reduces the time constant.

A more detailed analysis of the transient behavior has been undertaken and will be included in the final system report (Walker et al., 1992). Users will be able to acquire transient response data for each sensor. This will allow us to correct transient data obtained in the future rotating arm experiments for thermal capacitance lags.


## IX  Conclusions

It has been shown in this report that the local minimum in skin friction magnitude is approximately the location of a three-dimensional separation on the leeward side of a body with crossflow separation. If the relative crossflow momentum of the two boundary layers that converge at separation is much different, a single scheme is proposed in the Appendix for estimating the location of the separation, which will not coincide with the local minimum of skin-friction magnitude.

The relationship between the skin-friction magnitude and the heat transfer rate from a constant current anemometer sensor was derived and shows that the skin friction varies with the third power of the convective conductance. Thus, the convective conductance is a sensitive parameter for the detection of local minima in the skin-friction magnitude. The transient response of each sensor can be measured and used to correct measured data for time lags during transient flow conditions.

These sensors can be waterproofed by several means, but the best appears to be a uniform coating of a high thermal conductivity epoxy, which will also protect the sensors from abrasion.

Two series of measurements were performed to prove this concept. One set was performed in the VPI&SU Aerospace and Ocean Engineering Water Tunnel with a circular cylinder at 22° angle of attack. The second set was performed using a 6:1 prolate spheroid of 15° angle of attack in the David Taylor Research Center 140' Towing Basin. In both cases, measured separation locations agreed with those obtained in other experimental situations, except where flow conditions and interference were believed to be different.

Walker et al. (1992) will report complete documentation on all electronic circuits, sensor designs, and other details required for the operation of the kilo constant current anemometer for the DTRC rotating arm tests.

The success of this type of sensor for determining the relative convective conductance in water leads us to suggest that QUANTITATIVE convective conductance and skin friction results can be obtained if calibration of each TYPE of sensor is done with respect to known values. One possible calibration setup would be to use a fully-developed pipe flow of water.

# REFERENCES

Ahn, S. and Simpson, R. L. (1992) "Cross-flow Separation on a Prolate Spheroid at Angles of Attack," AIAA 92-0428, 30th Aerospace Sciences Meeting and Exhibit, Jan. 6-9, Reno, NV.

Crowder, J. (1980) "Add Fluorescent Minitufts to the Aerodynamicist's Bag of Tricks," *Aeronautics and Astronautics,* Vol. 18, pp. 54-56.

Feyzi, F., Kornberger, M., Rachor, N., and Ilk, B. (1989) "Development of Two Multi-sensor Hot-film Measuring Techniques for Free-Flight Experiments," Proceedings of the International Congress on Aerospace Instrumentation and Simulation Facilities, IEEE, Goettingen, W. Germany, pp. 443-449.

Holman, J. P. (1989) *Experimental Methods for Engineers,* 5th Edition, McGraw-Hill Book Co., N.Y.

Holman, J. P. (1990) *Heat Transfer,* 6th Edition, McGraw-Hill Book Co., N.Y.

Kreplin, H.-P., Vollmers, H. and Meier, H. U. (1982) "Measurements of the Wall Shear Stress on an Inclined Prolate Spheroid, *Z. Flugwiss. Weltraumforsch.,* 6 (1982), Heft 4, pp. 248-252.

Kreplin, H.-P., Vollmers, H., and Meier, H.-U. (1985) "Shear Stress Measurements on an Inclined Prolate Spheroid in the DFVLR 3m X 3m Low Speed Wind Tunnel, Goettingen - Data Report," DFVLR Report IB 222-84 A 33.

Maskell, E. C. (1955) "Flow Separation in Three Dimensions," RAE Aero. Report 2565.

Meier, H. U. and Kreplin, H.-P. (1980) "Experimental Investigation of the Boundary Layer Transition and Separation on a Body of Revolution," *Z. Flugwiss. Weltraumforsch.,* 4, Heft 2, pp. 65-71.

Moskovitz, C. A. and Simpson, R. L. (1990) "Detection of Three-Dimensional Separation from Submarine Surfaces During a Turning Maneuver," Final Report, VPI-AOE-166, Aerospace and Ocean Engineering Dept., VPI&SU.

Poll, D.I.A. (1985) "On the effect of boundary-layer transition on a cylindrical afterbody at incidence in low-speed flow," *Aero. J.,* Oct., pp. 315-327.

Simpson, R. L., (1985) "Two-Dimensional Turbulent Separated Flow", NATO-AGARD Report AG-287-Vol. 1.

Tobak, M. and Peake, D. (1982) "Topology of Three-Dimentional Separated Flows," *Ann. Rev. Fluid Mech.,* Vol. 14, pp. 61-85.

Vollmers, H., Kreplin, H.-P., and Meier, H. U. (1983) "Separation and Vortical-Type

Flow Around a Prolate Spheroid - Evaluation of Relevent Parameters," paper 14 in, "Aerodynamics of Vortical-Type Flows in Three Dimensions," AGARD-CP-342.

Walker, D. A., Shinpaugh, K. A., and Simpson, R. L. (1992) "Documentation Report for the Kilo Constant Current Anemometer Three-Dimensional Separation Location System," VPI-AOE-187 Aerospace and Ocean Engineering Dept., VPI&SU, in preparation.

## APPENDIX A

## THE RELATIONSHIP OF SURFACE PARAMETER PARAMETERS
## TO THE LOCATION OF THREE-DIMENSIONAL SEPARATION LINES

Along a three-dimensional separation line on the surface of a body rises a stream surface, across which no flow from one side of the separation line can pass to the other side. Fluid moves away from the wall with a relatively large normal-to-wall velocity component $V$ at the separation stream surface. As also shown in Figure 1, surface skin friction lines converge on each side of the separation line, as well as converge toward one another (Tobak and Peake, 1982). We observe that low velocity near wall fluid from each side of the separation line flows toward the separation line, so a local minimum in skin friction magnitude must occur in the vicinity of the separation line. Here we examine the governing equations and other features of the shear stress in order to relate the behavior of surface parameters to the location of separation.

We can examine the *continuity* and *momentum* equations on the surface for an incompressible flow. From continuity we obtain

$$\frac{\partial V}{\partial y}\bigg|_W = -\left(\frac{\partial U}{\partial x} + \frac{\partial W}{\partial z}\right)_W = 0 \qquad (A.1)$$

The momentum equation yields

$$\frac{\partial P}{\partial x} = \mu \frac{\partial^2 U}{\partial y^2} \qquad (A.2)$$

and

$$\frac{\partial P}{\partial z} = \mu \frac{\partial^2 W}{\partial y^2} \qquad (A.3)$$

At the surface the shear stress vector is given by

$$\vec{\tau}_W = \tau_{wx}\vec{i} + \tau_{wz}\vec{j} = \mu\left(\frac{\partial U}{\partial y}\vec{i} + \frac{\partial W}{\partial y}\vec{j}\right) \qquad (A.4)$$

The divergence of the shear stress vector on the wall is

$$\vec{\nabla} \cdot \vec{\tau}_w = \mu\left(\frac{\partial^2 U}{\partial x \partial y} + \frac{\partial^2 W}{\partial y \partial z}\right) = -\mu \frac{\partial^2 V}{\partial y^2}\bigg|_W \qquad (A.5)$$

where the continuity equation has been used to obtain the last expression. The direction of the surface shear stress vector, and therefore the direction of the shear stress vector coincident with the separation line, is given by the expression

$$\theta = \tan^{-1}(\tau_{wz}/\tau_{wx}) \qquad (A.6)$$

Derivatives of equation (A.2) and (A.3) produce

$$\nabla^2 p = \mu \frac{\partial^3 V}{\partial y^3}\bigg|_W \qquad (A.7)$$

Thus, the near wall normal-to-wall velocity component can be expressed in a Taylor series using only surface parameters for the first few terms.

$$V = \frac{\partial^2 V}{\partial y^2}\bigg|_w \frac{y^2}{2} + \frac{\partial^3 V}{\partial y^3}\bigg|_w \frac{y^3}{6} + \cdots \qquad (A.8)$$

or

$$V = -\frac{1}{2\mu}(\vec{\nabla} \cdot \vec{\tau}_w)y^2 + \frac{1}{6\mu}(\nabla^2 P)y^3 + \cdots \qquad (A.9)$$

Clearly, we see that the surface shearing stress contributes lower order information to the location of a separation line. Equation (A.5) relates the second derivative of the velocity component normal to the surface to the divergence of the wall shear stress obtained on the wall. Only the third and higher derivatives of the wall pressure field are related to the velocity component normal to the wall. Therefore, wall pressure measurements are relatively insensitive to the phenomena of separation. Only "massive" separations are detected from wall pressure measurements (Vollmers et al., 1982).

Note that even with the wall shear stress, one must have complete data over the surface in order to perform the divergence operation and locate where the normal-to-the-wall velocity component is relatively large and thus the location of the separation line. The impracticality of an extremely large number of shear stress sensors leads us to consider an APPROXIMATE method for locating separation lines with fewer shear stress sensors.

To a first approximation, the separation line will be in the vicinity of the local minimum in the shear stress magnitude. We cannot rigorously say how close the local minimum is to the actual separation line, except for the special case where the converging shear flows and their surface shear stress distributions on each side of the minimum are symmetric. In that case the symmetry requires that the local minimum in shear stress magnitude be coincident with the separation line.

An example will serve to show how well this approximate method works for crossflow separation. Figure A.1 shows distributions of the surface shearing stress magnitude and direction at various axial locations on a 6:1 prolate spheroid at 30° angle of attack (Kreplin et al., 1982). (One must not confuse the local minimum that occurs near transition from

laminar flow to turbulent flow on the windward side ($\phi < 90°$) as a three-dimensional separation.)

Figure A.2 shows the locations of the first local minima in surface shear stress magnitude on the leeward side as a function of axial length along the body as determined from these data (Meier and Kreplin, 1980). As pointed out by Meier and Kreplin, if one takes into account that the oil flow pattern must lead to a primary flow separation at lower circumferential angles $\phi$, the agreement with hot-film shear stress results is good. However, Meier and Kreplin did not point out that the agreement with the oil flow results was best where the shear stress magnitude distributions were more symmetric about the minimum, i.e., for $0.3 < x/2a < 0.7$. For $x/2a > 0.8$, Figure A.2 shows a larger deviation of the shear stress minimum location from the oil flow results while Figure A.1 shows rather unsymmetric shear stress distributions about the minimum.

This leads us to propose a refinement in locating the separation. Figure A.3 illustrates two cases, the one where the shear stress distribution is symmetric about the minimum, and a second where it is not. In the latter case, it is clear that the near wall velocities of the flow converging from the left are greater, having greater momentum toward the separation line and pushing the minimum shear stress magnitude toward the lower velocity right side of the separation. This means that the minimum shear stress location is closer to the lower velocity fluid than the actual separation line.

It appears that the maximum $(\partial \tau_w / \partial \phi)_{max}$ and minimum $(\partial \tau_w / \partial \phi)$ slopes of the shear stress magnitudes nearest the minimum in shear stress magnitude can be used as measures of the relative momentum of the two converging streams. If so, then we can propose to locate the separation line where the maximum and minimum slope lines converge, as shown in Figure A.3 and given by

$$\phi_{sep} = -\frac{(\tau_{WB} - \tau_{WA}) + S_B \phi_B - S_A \phi_A}{(S_B - S_A)} \qquad (A.10)$$

Of course, for cases where the shear stress distributions are symmetric about the minimum, such as case 1 in Figure A.3, the results from equation (A.10) are coincident with the minimum in shear stress magnitude. Figure A.2 shows the results obtained using equation (A.10) for the Kreplin, et al. data. Note the better agreement with the oil flow results for $x/2a > 0.6$.

In conclusion, to determine the approximate location of crossflow separation, one must have at least enough shear stress sensors around the perphery of a model to define the local minimum and define the nearby maximum and minimum slopes of the shear stress magnitude.

23

## LIST OF FIGURES

24

Figure A.2   Comparison of separation regions obtained from oil flow patterns and surface hot film measurements, $\alpha = 30°$ (Meier and Kreplin, 1980). Circles denote location of local minimum in skin friction magnitude. Squares denote separation locations calculated by equation (A.10) and the method shown schematically in Figure A.3.

Figure A.3   Examples of variations of the wall shear stress magnitude in the vicinity of a local minimum:

(a) example of locally symmetric distribution of $|\tau_W|$ around a shear stress minimum.

(b) example of locally asymmetric distribution of $|\tau_W|$ around a shear stress minimum.

VISCOUS REGION

SURFACE OF SEPARATION

STREAMLINE IN EXTERNAL STREAM

E

E

LIMITING STREAMLINES

SURFACE OF SOLID BODY

Figure 1. Schematic diagram of a three-dimensional open separation (Maskell, 1955).
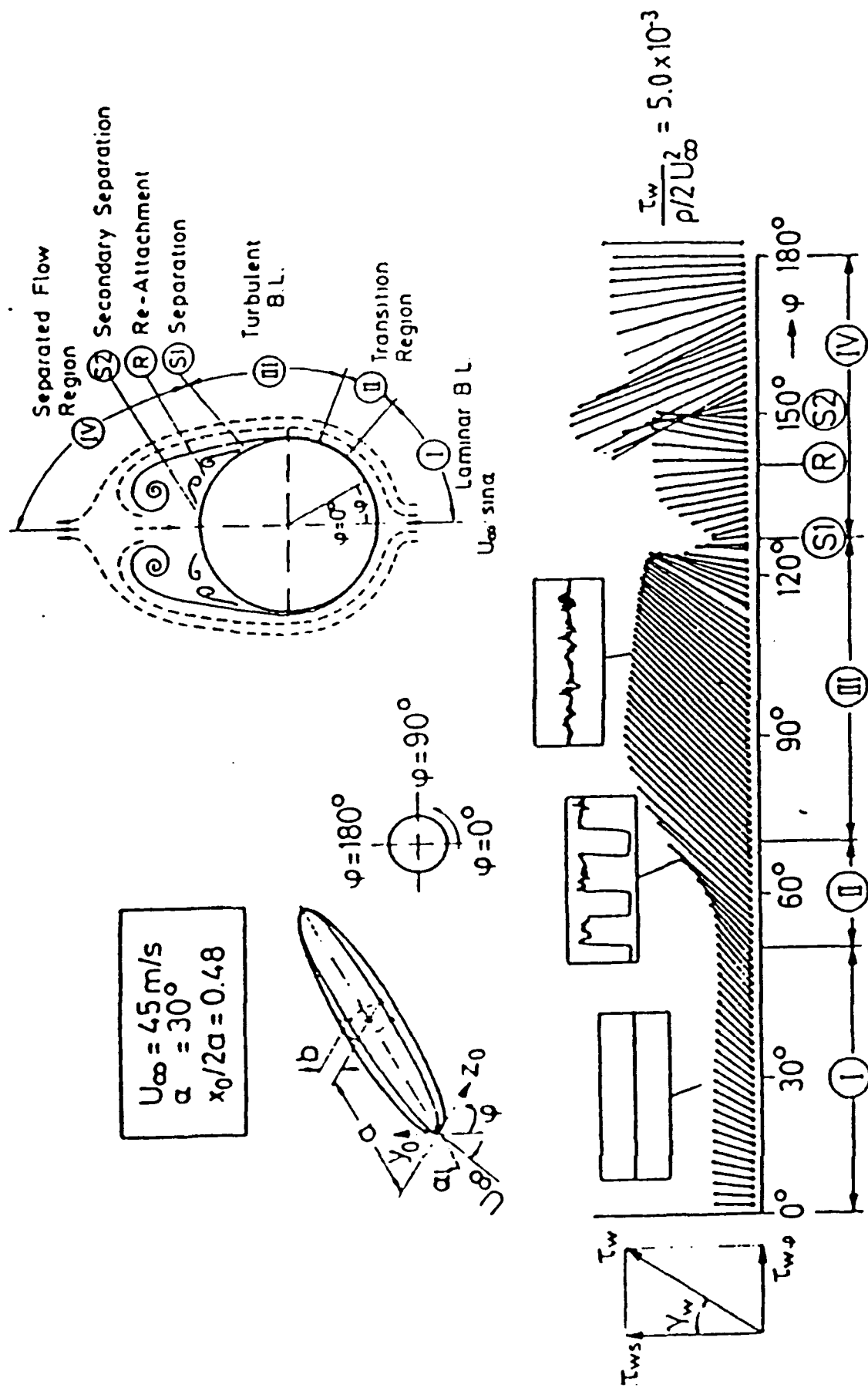
Figure 2. Experimental measurements of the magnitude and direction of the mean wall shear stress at one axial location on a 6:1 prolate spheroid (Kreplin et al., 1982).
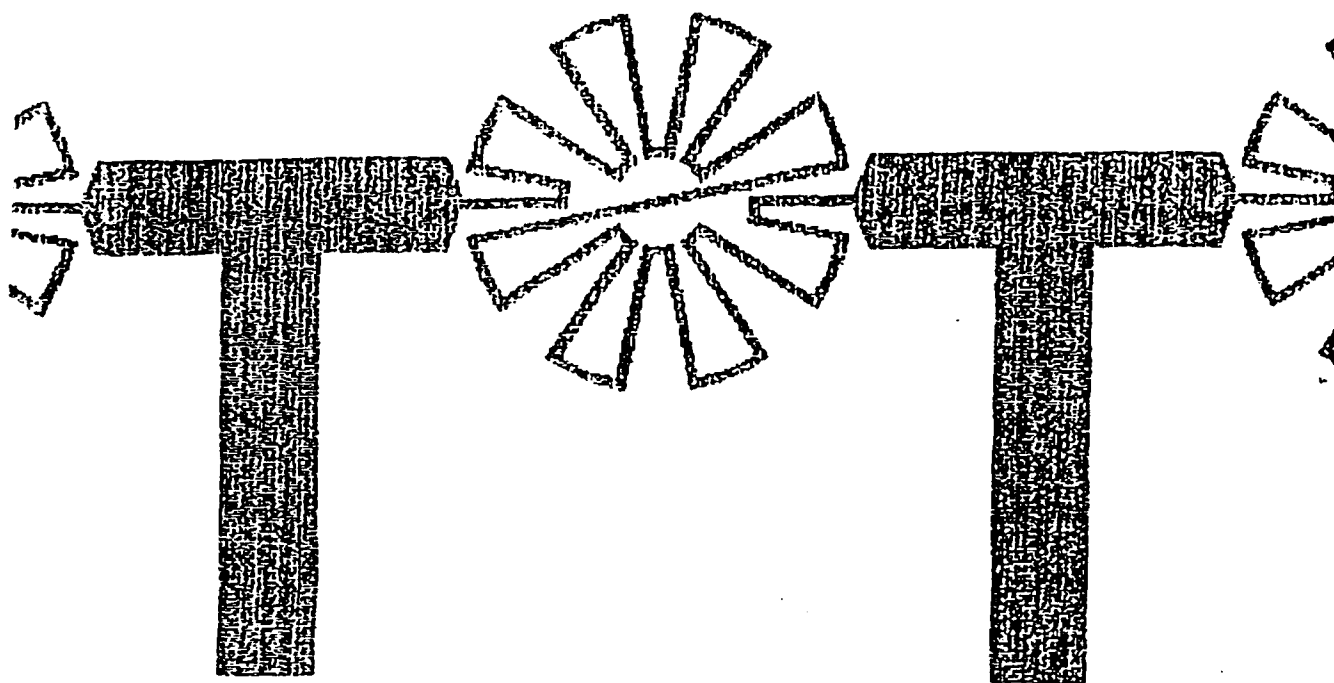
Figure 3.    Shape of the balco foil sensing element used in the MINCO sensor (8 times actual size).
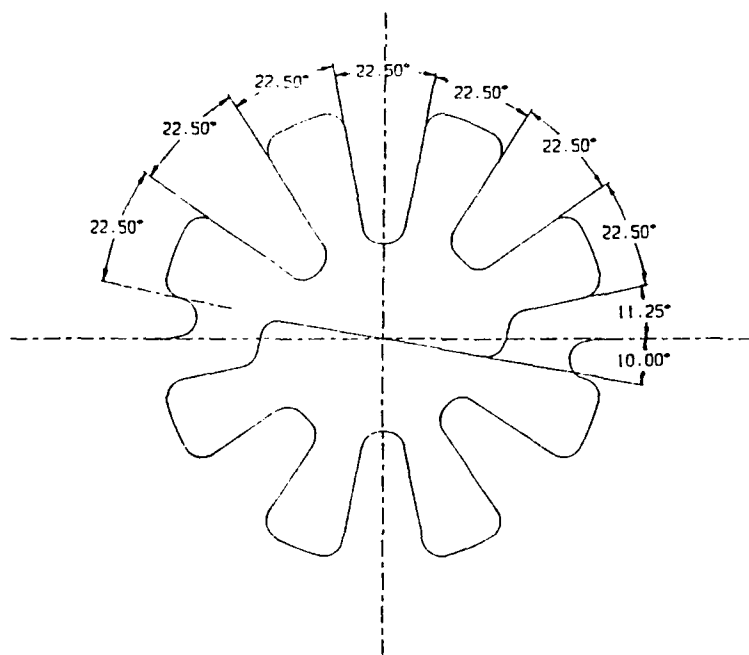


Figure 4.    Shape of the Advance Circuit Systems balco foil sensing element (8 times actual size).

Water flow over sensor



fiberglas model
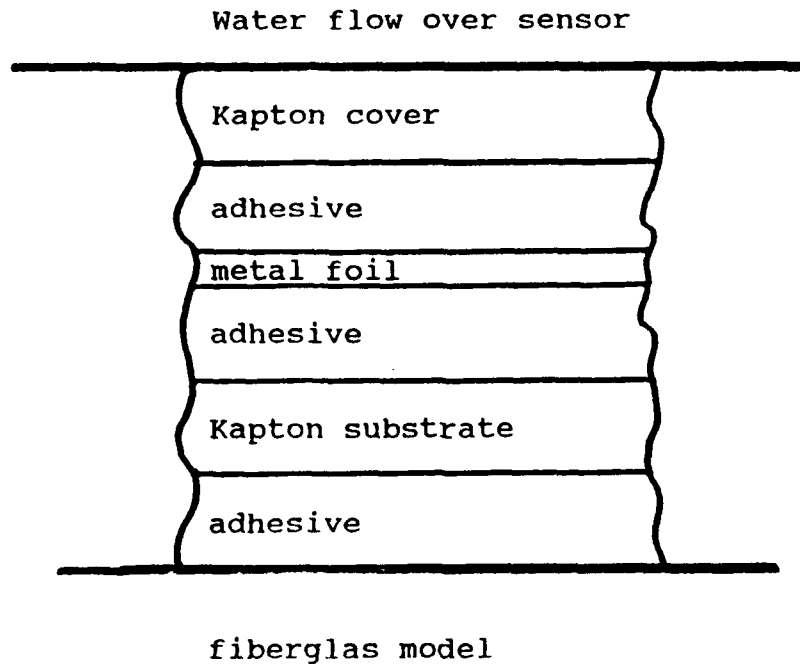
Figure 5.     Schematic of the sensor cross-section.

Table 1. Some properties of materials used in the MINCO sensors as supplied by MINCO.

| material | resistivity, $\mu\Omega$-cm | thermal conductivity, $W/m-^0C$ | temperature coefficient of resistivity, $^0C^{-1}$ |
|---|---|---|---|
| Kapton polyamide | $10^{24}$ | 0.98 | 30 to 60 x $10^{-6}$ |
| Balco foil 70% Ni,30% Fe | 19.9 | 200. | 0.0051 |
| Pyralux adhesive | $10^{20}$ to $10^{24}$ | 0.22 | < $10^{-5}$ |
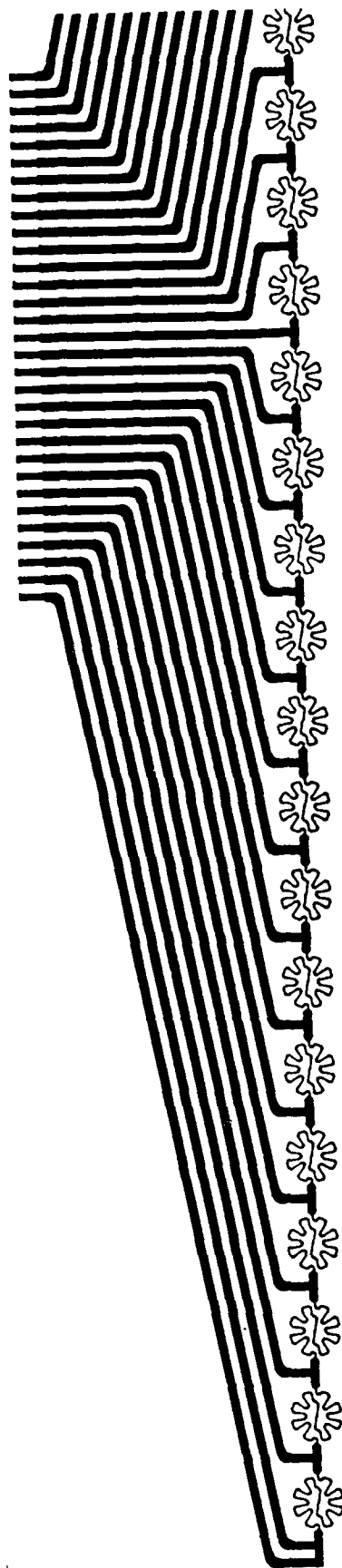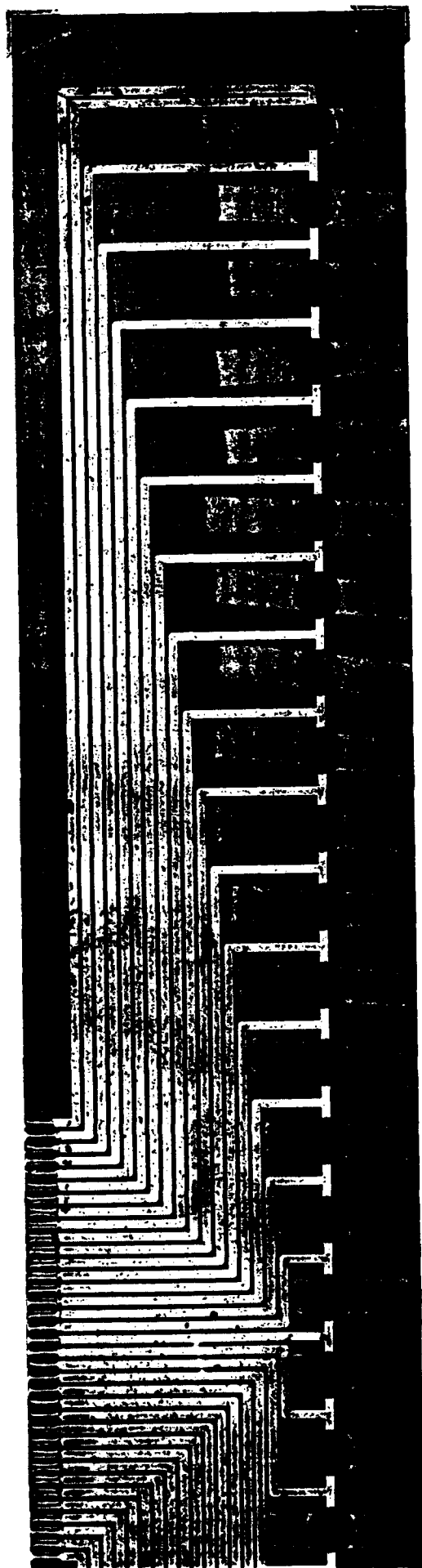
Figure 6.  (a) Strip of MINCO sensors (actual size);  (b) Strip of Advance Circuit Systems sensors (actual size).

# Calibration of Constant Current Source
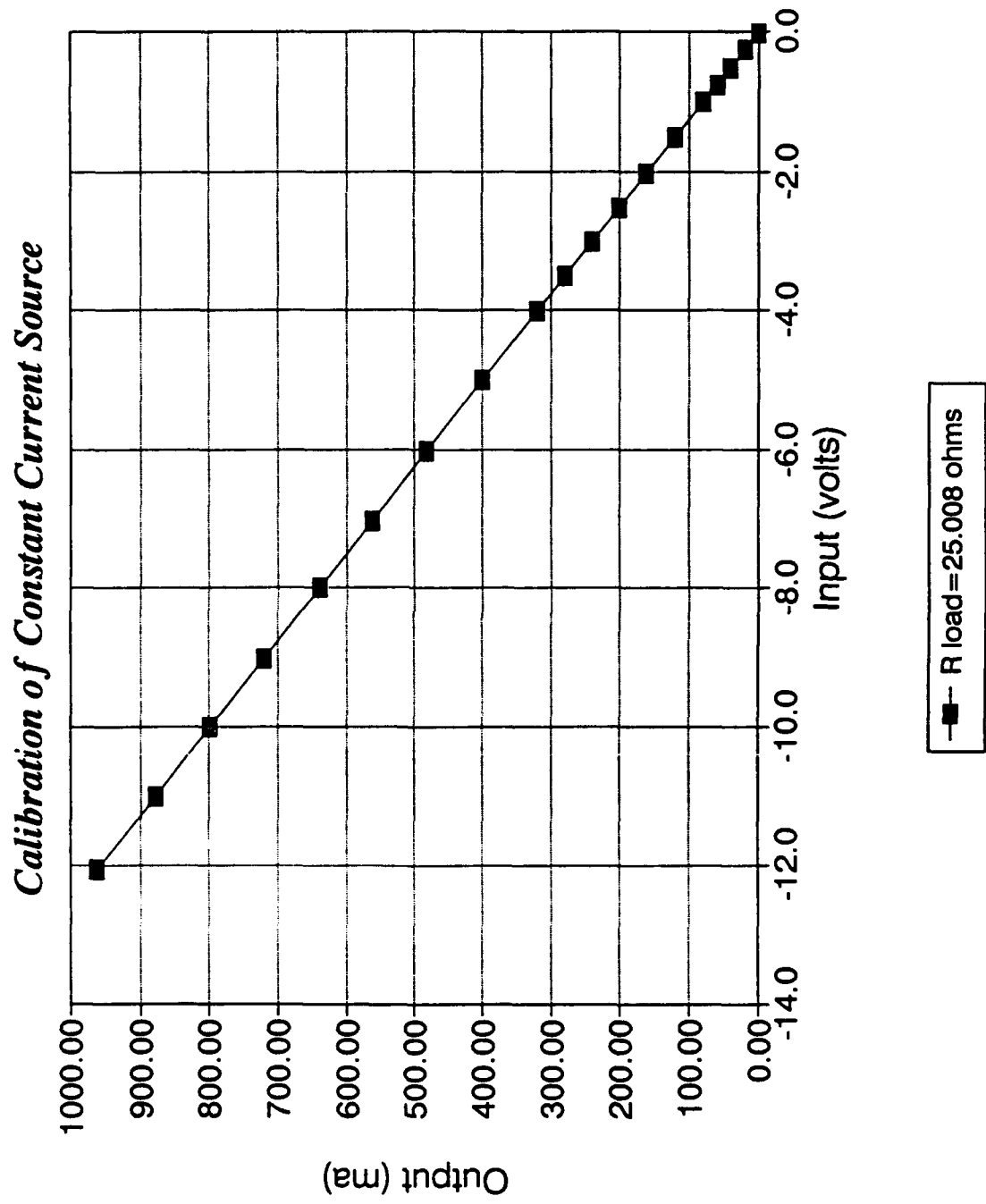


Figure 7.    Current source calibration used in the DTRC 140' Towing Basin tests.
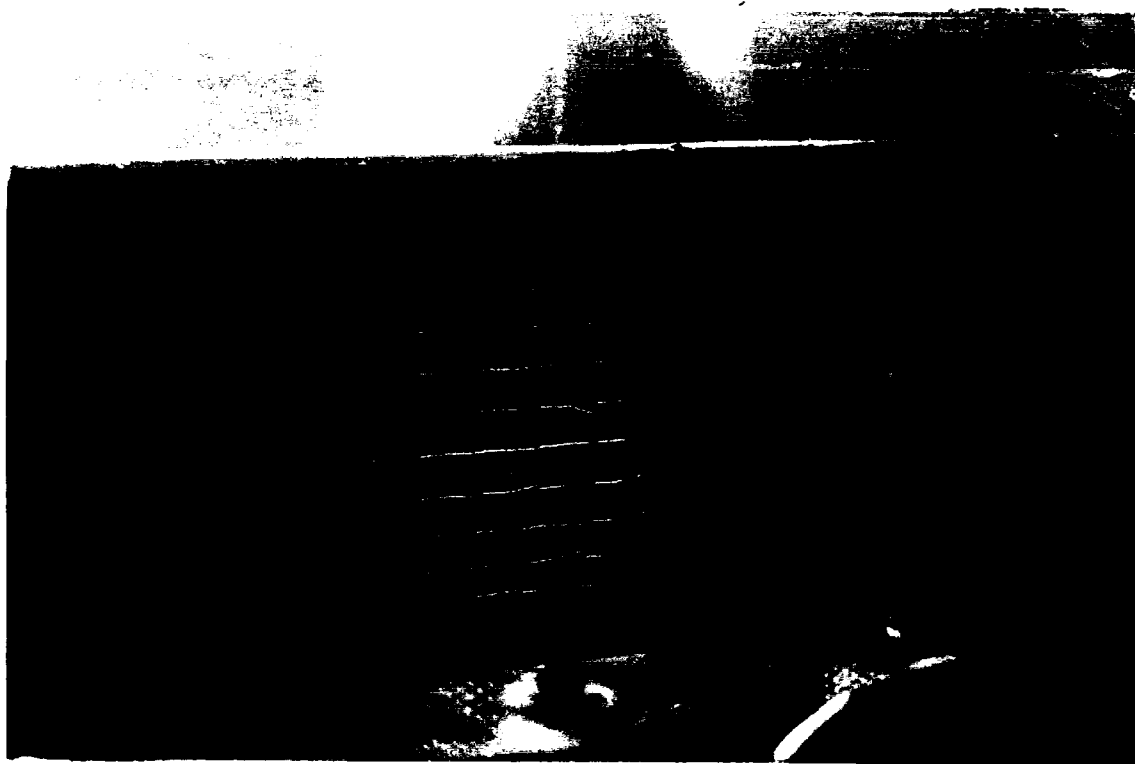
Figure 8a.    Photograph of ultra–violet illuminated "mini-tufts" mounted on a circular cylinder at 0 degrees angle-of-attack in the VPI&SU Water Tunnel.
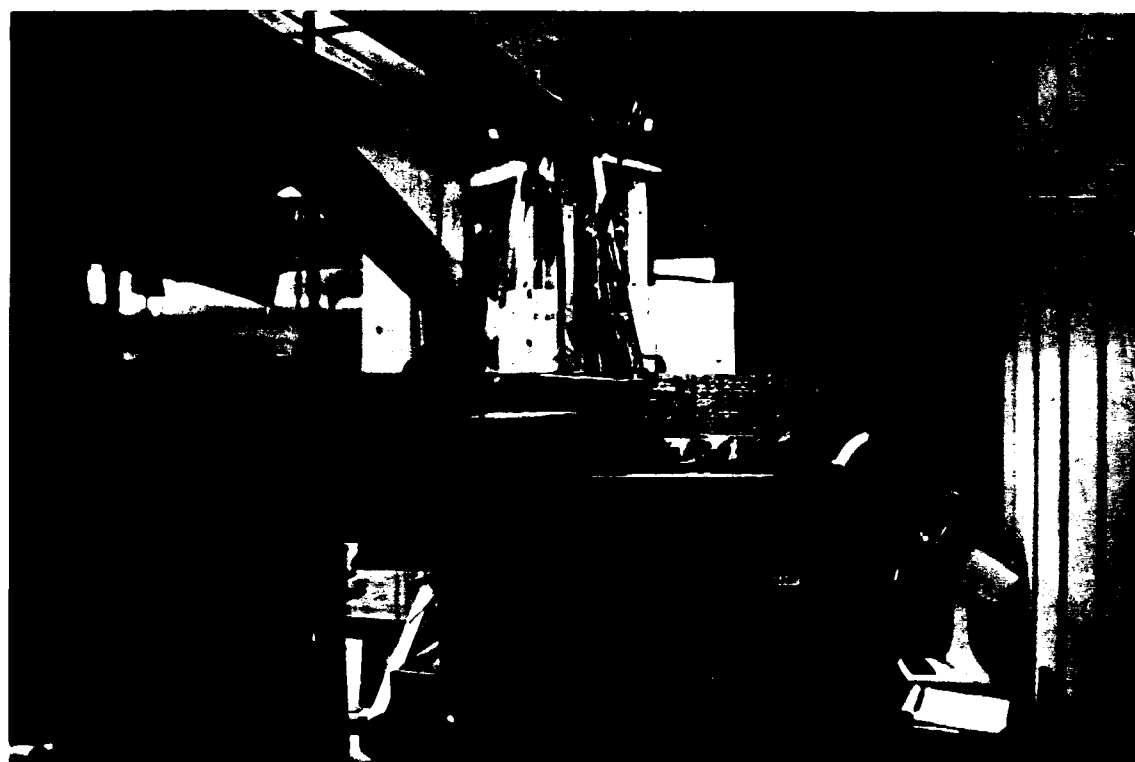


Figure 8b.    Photograph of the apparatus in the VPI&SU Water Tunnel for the circular cylinder at 22 degrees angle-of-attack tests of the constant current anemometer separation location system.

Figure 8c.    Photograph of the 6.625" diameter circular cylinder in the VPI&SU Water
Tunnel at 22 degrees angle of attack.
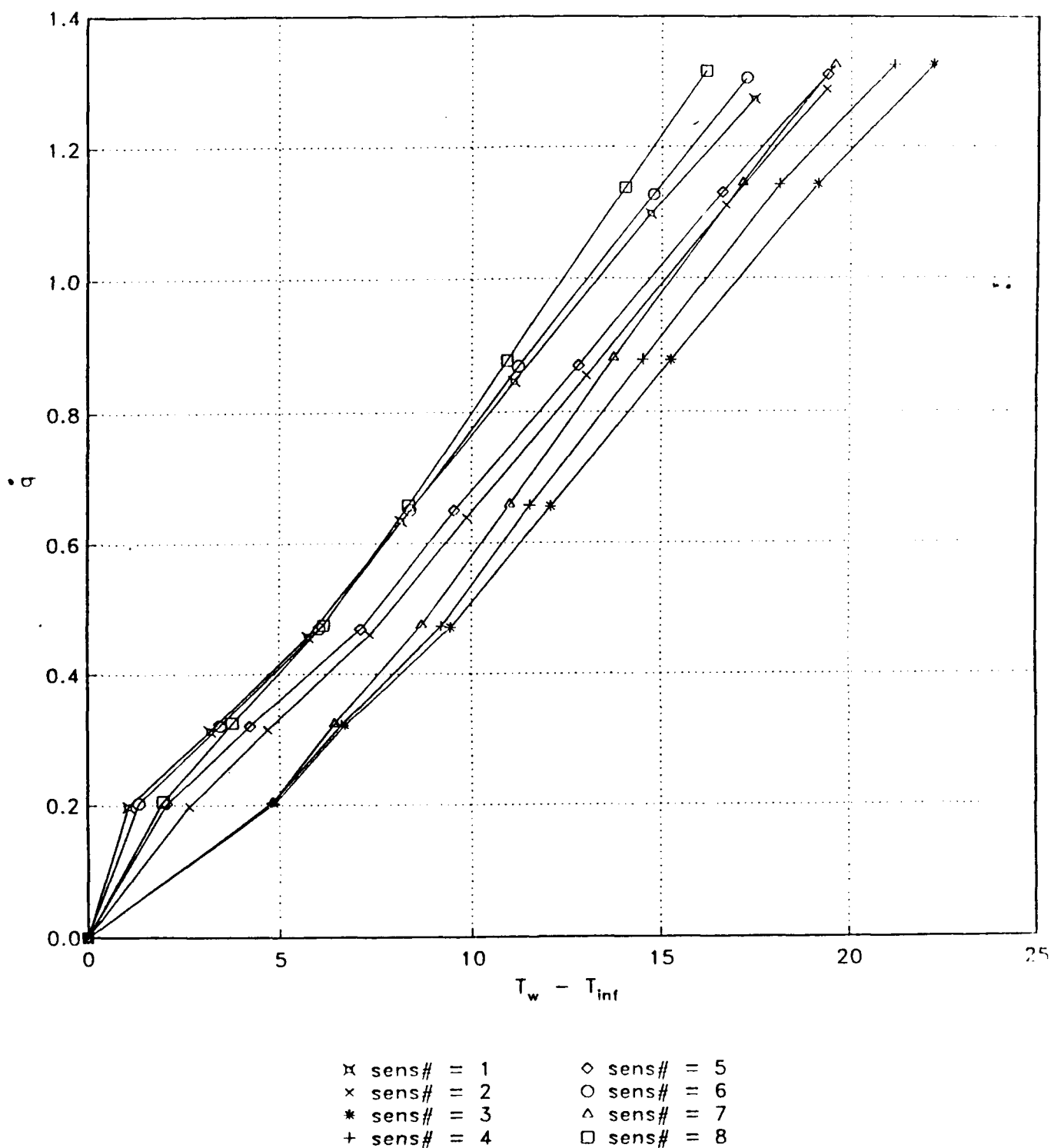
Figure 9.    Experimental data for the circular cylinder at 22 degrees angle of attack. Measured heat transfer rate, $\dot{q}$, for each of 8 constant current anemometer sensors is plotted versus the sensor cover temperature difference, $(T_w - T_\infty)$, for each of 8 different current settings.
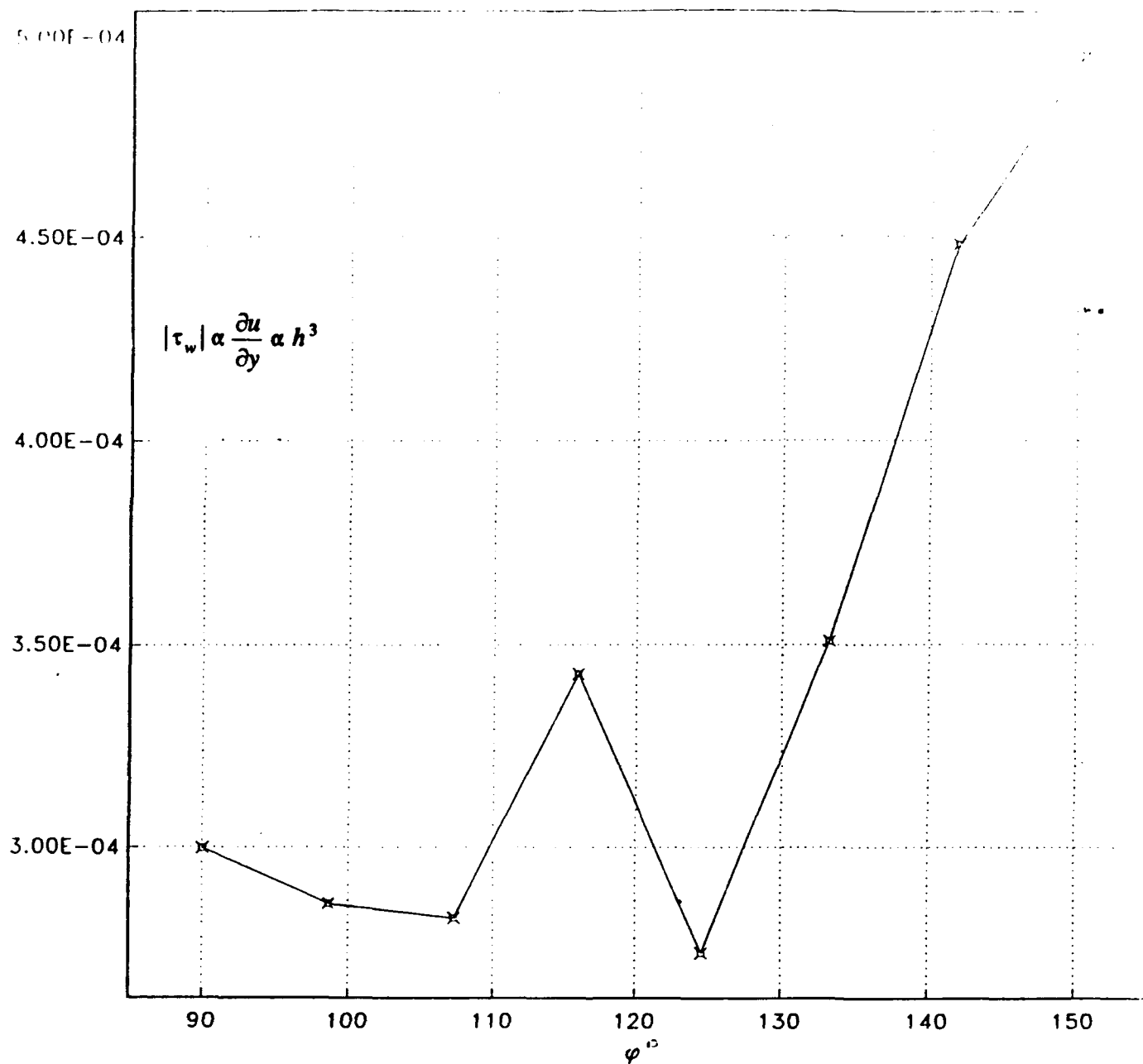
Figure 10.    Experimental results of the relative magnitude of the surface shearing stress versus the peripheral angle. Note the location of a separation near 105°, a reattachment near 115°, and a second separation near 125°.
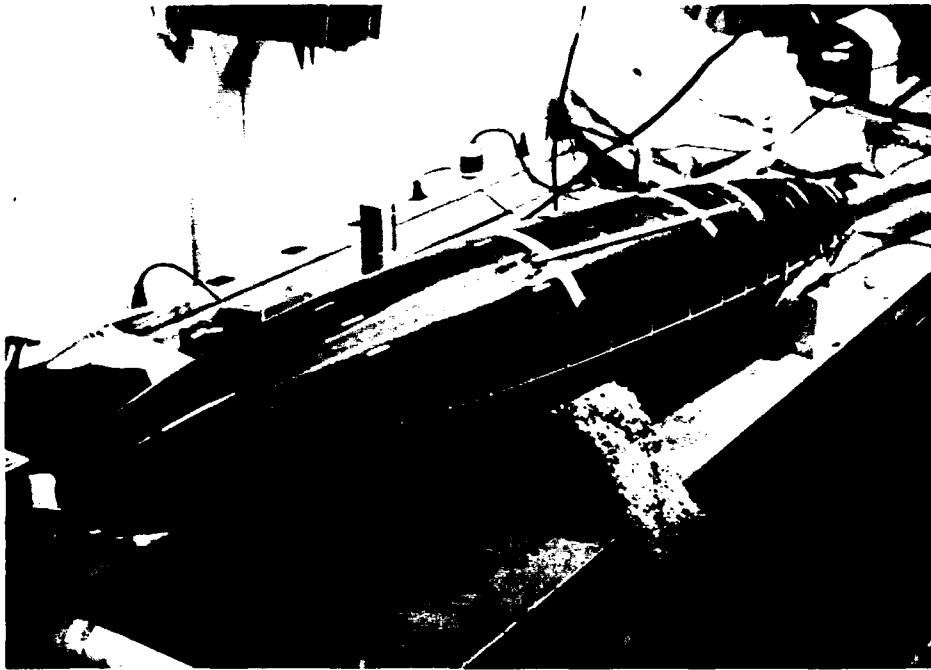
Figure 11.   Photograph of the 54" long 6:1 prolate spheroid with the sting shown at the right.



Figure 12.   Photograph of the nose of the 6:1 prolate showing the 1/16" diameter trip wire located at x/C=0.2.

Figure 13. Photograph of three strips of sensors located at x/C=0.7, 0.8, and 0.9 on the 6:1 prolate spheroid.
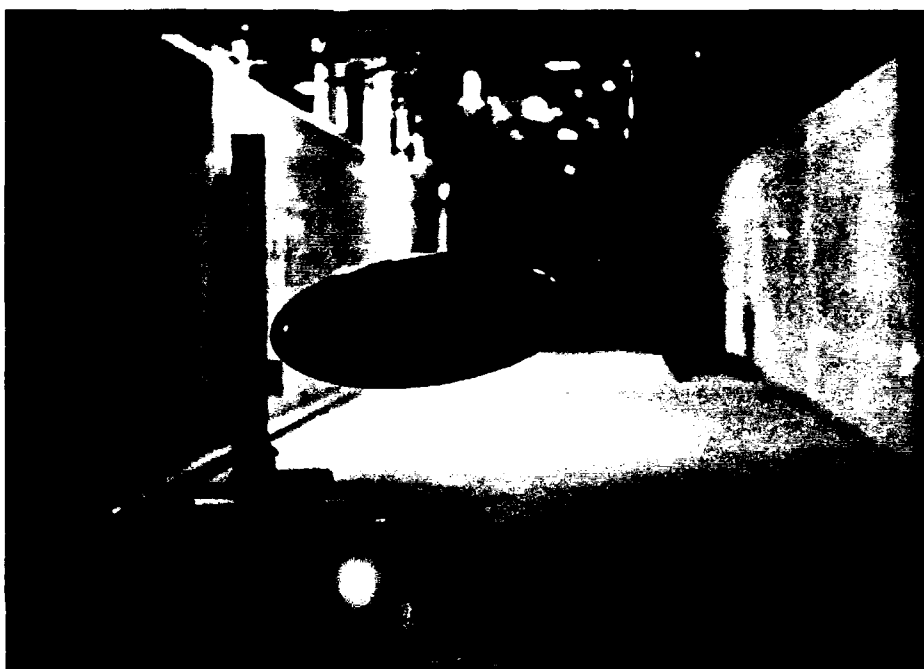


Figure 14. Photograph of the prolate spheroid model mounted on the sting of the carriage for the DTRC 140' Towing Basin.
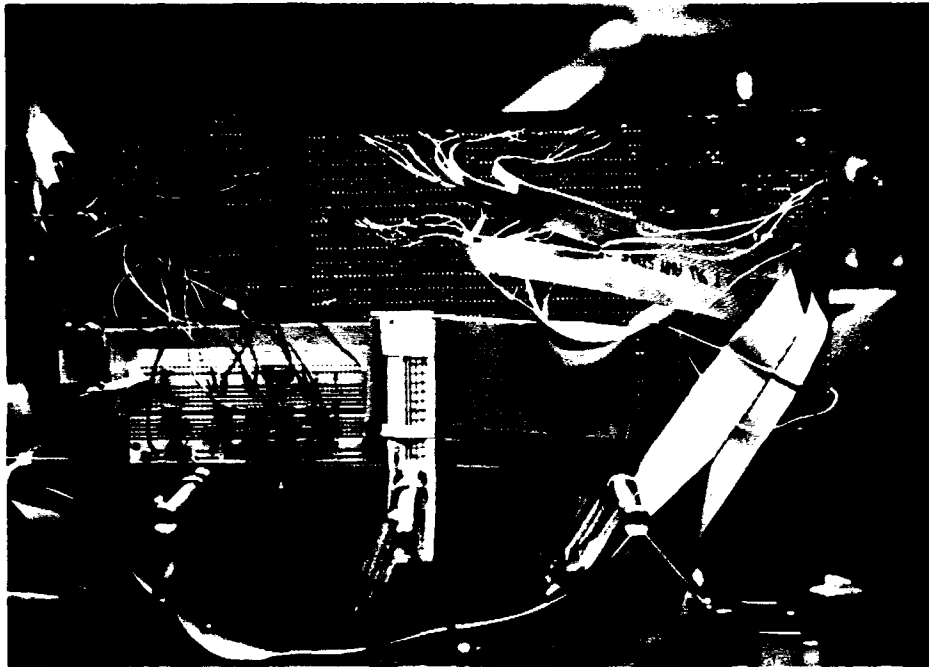
Figure 15.     Photograph of the constant current source and amplifier board used in the 140' Towing Basin tests.
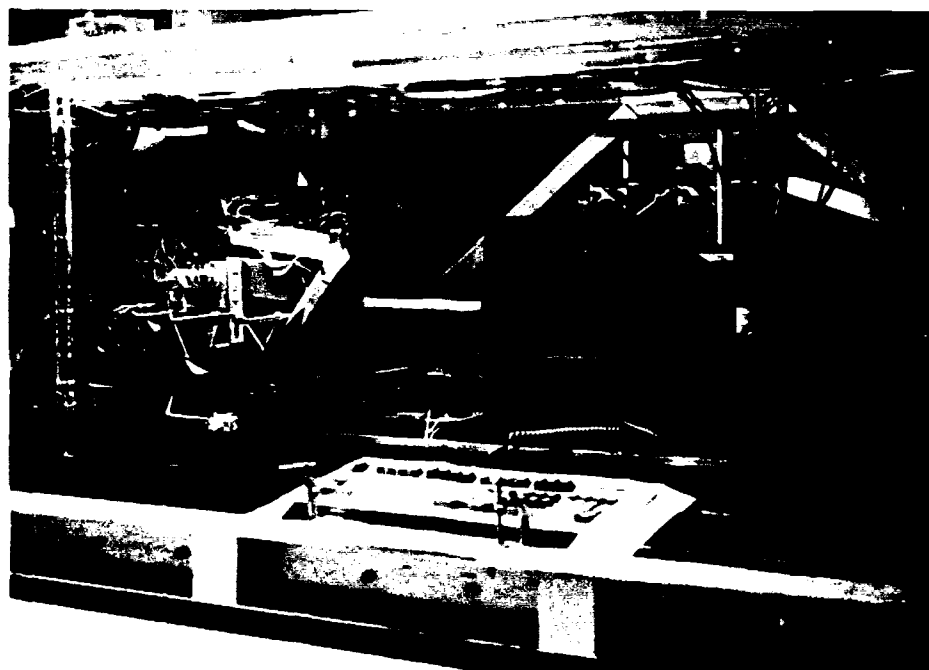


Figure 16.     Photograph of the constant current anemometer board and data acquisition computer mounted on the carriage of the 140' Towing Basin.
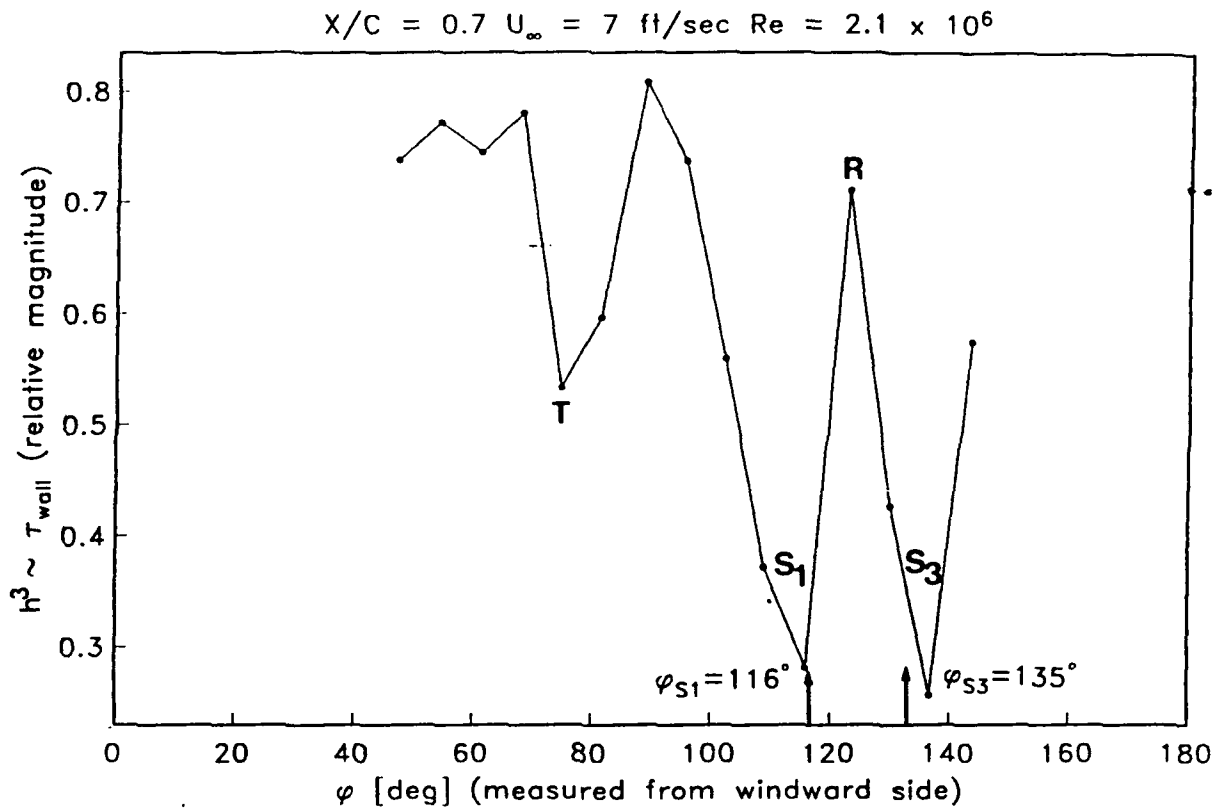
X/C = 0.7  U∞ = 5 ft/sec  Re = 1.5 × 10⁶
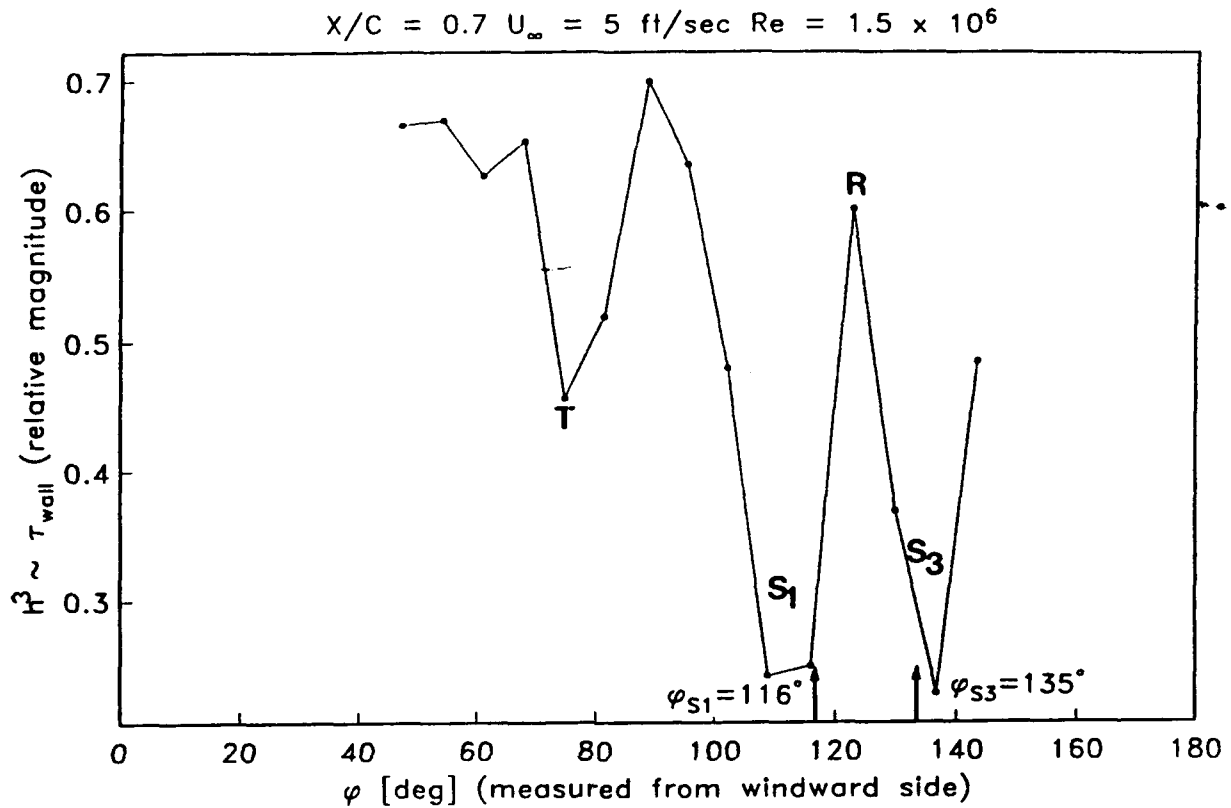
Figure 17.   Relative magnitude of the surface shear stress at x/C=0.7 at peripheral an-
gles measured from the windward side for the 5 fps flow over the prolate
spheroid at 15 angle of attack. $T$ denotes location of transition on the wind-
ward side; $R_1$ denotes reattachment location; $S_1$ denotes location of primary
separation; $S_3$ denotes location of tertiary separation. Primary and tertiary
separation from wind tunnel data at Re = 2.85 × 10⁶ are indicated by arrows
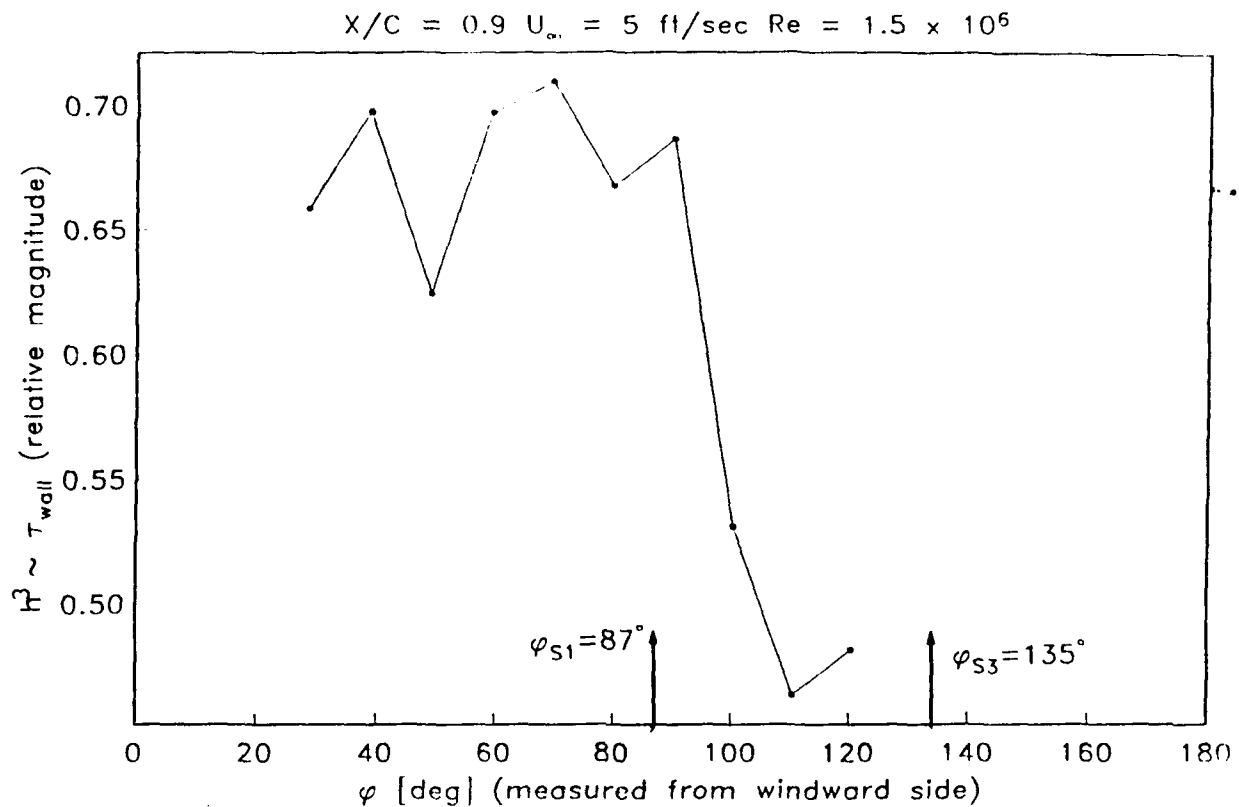and angular values (Ahn and Simpson, 1992).

X/C = 0.7  U∞ = 7 ft/sec  Re = 2.1 x 10⁶

Figure 18.   Relative magnitude of the surface shear stress at x/C= 0.7 at peripheral angles measured from the windward side for the 7 fps flow over the prolate spheroid at 15 angle of attack. $T$ denotes location of transition on the windward side; $R_1$ denotes reattachment location; $S_1$ denotes location of primary separation; $S_3$ denotes location of tertiary separation. Primary and tertiary separation from wind tunnel data at Re = 2.85 x 10⁶ are indicated by arrows and angular values (Ahn and Simpsor, 1992).
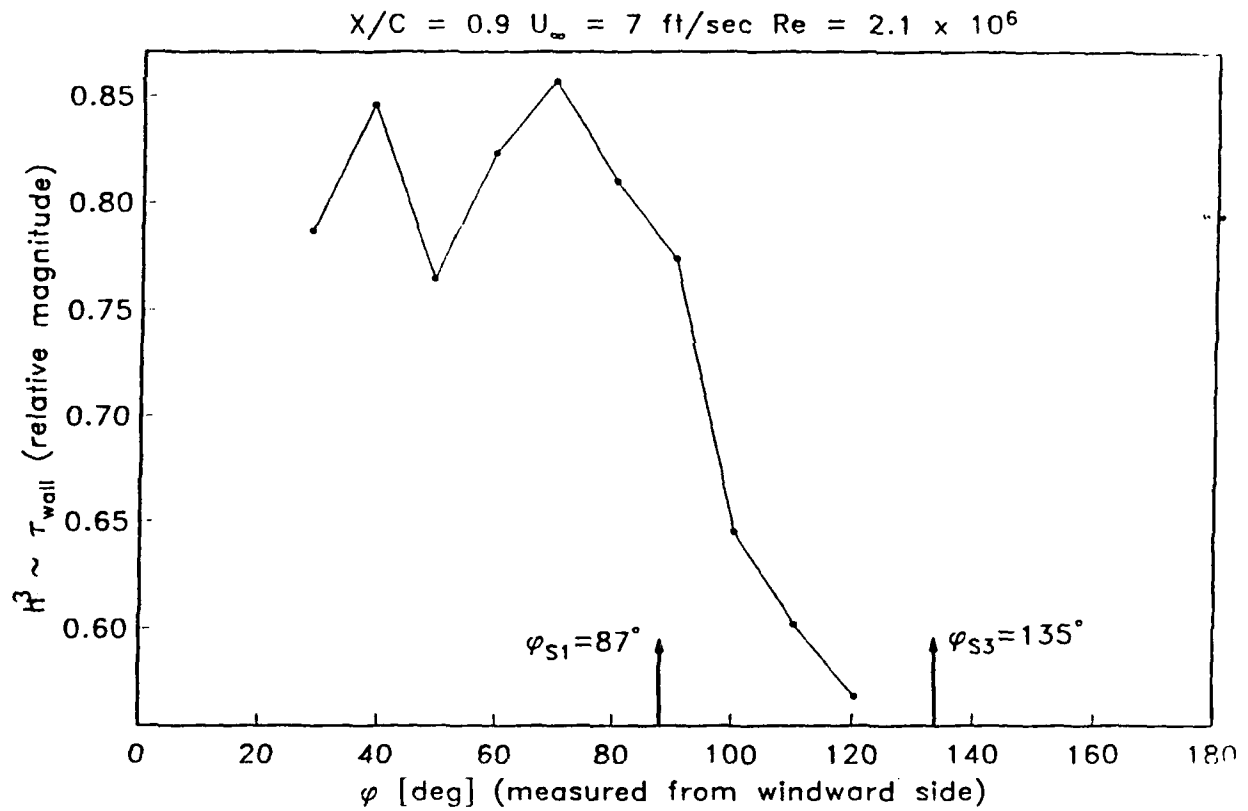
X/C = 0.9  U∞ = 5 ft/sec  Re = 1.5 × 10⁶

Figure 19.    Relative magnitude of the surface stress at x/C = 0.9 at peripheral angles measured from the windward side for the 5 fps flow over the prolate spheroid at 15 angle of attack. $T$ denotes location of transition on the windward side; $R_1$ denotes reattachment location; $S_1$ denotes location of primary separation; $S_3$ denotes location of tertiary separation. Primary and tertiary separation from wind tunnel data at Re = 2.85 × 10⁶ are indicated by arrows and angular values (Ahn and Simpson, 1992).

Figure 20. Relative magnitude of the surface stress at x/C = 0.9 at peripheral angles measured from the windward side for the 7 fps flow over the prolate spheroid at 15 angle of attack. $T$ denotes location of transition on the windward side; $R_1$ denotes reattachment location; $S_1$ denotes location of primary separation; $S_3$ denotes location of tertiary separation. Primary and tertiary separation from wind tunnel data at Re = 2.85 x $10^6$ are indicated by arrows and angular values (Ahn and Simpson, 1992).
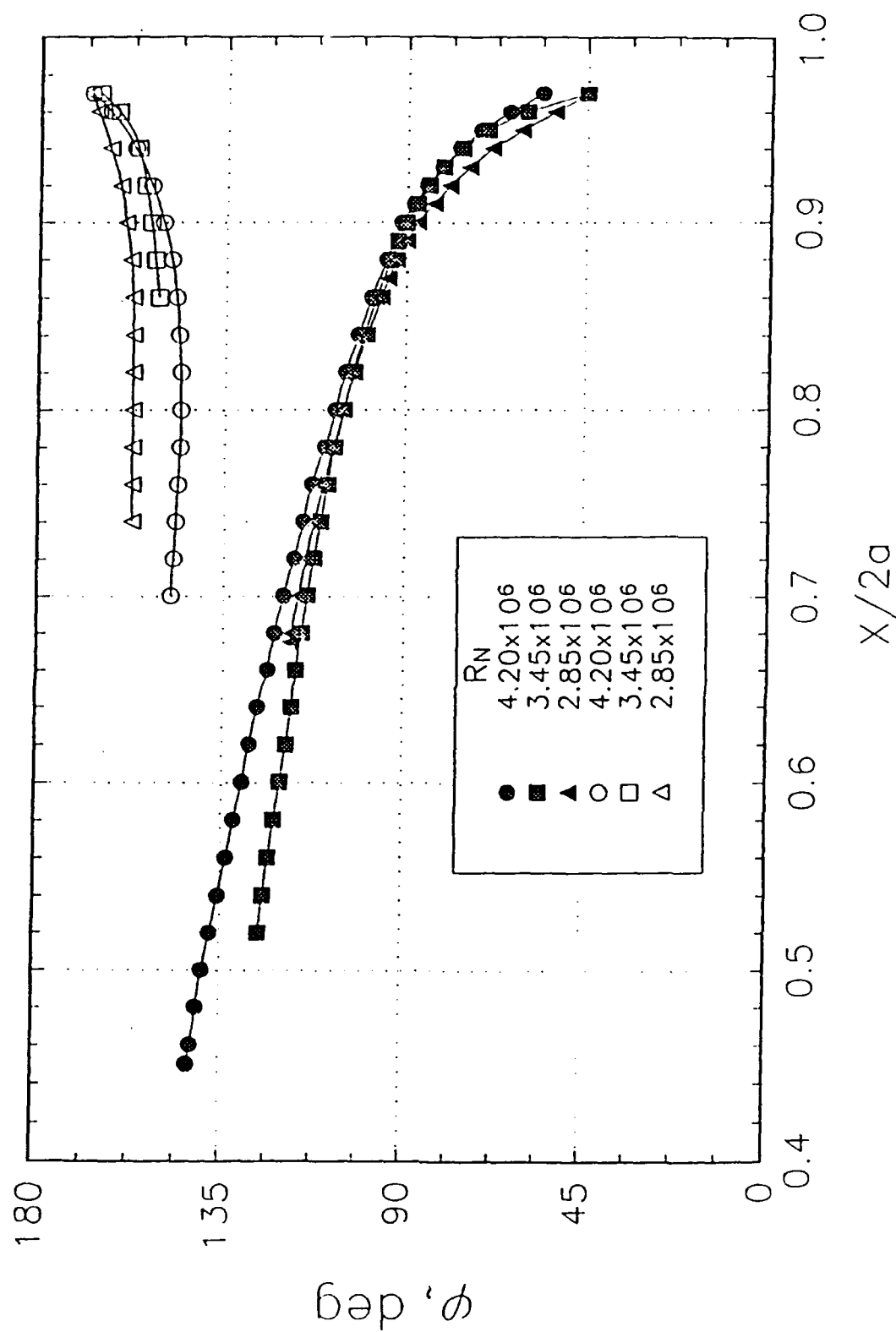
Figure 21. Separation lines at different Reynolds numbers at $\alpha = 15°$. Closed symbols denote primary separation and open symbols denote secondary separation. (Ahn and Simpson, 1992).
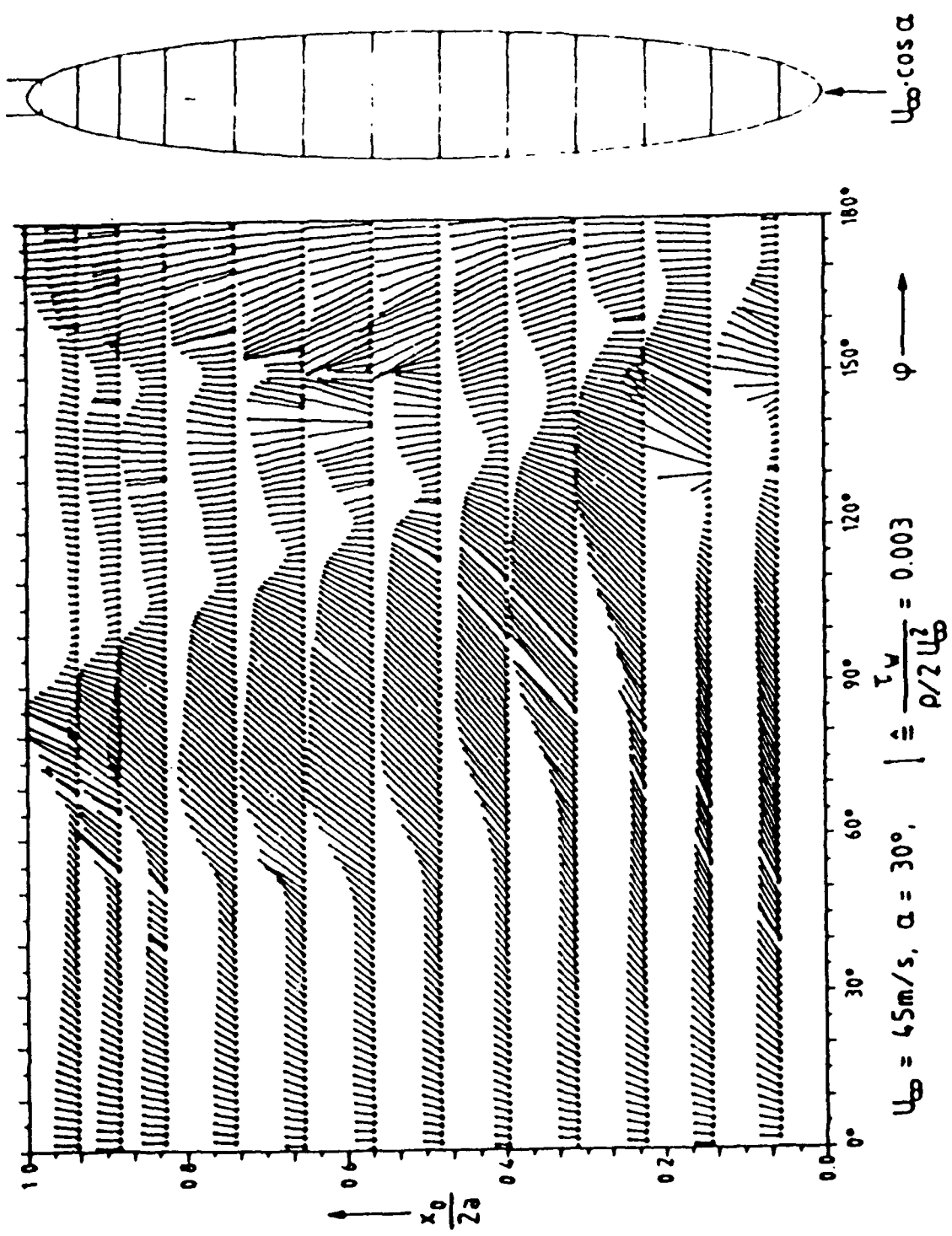
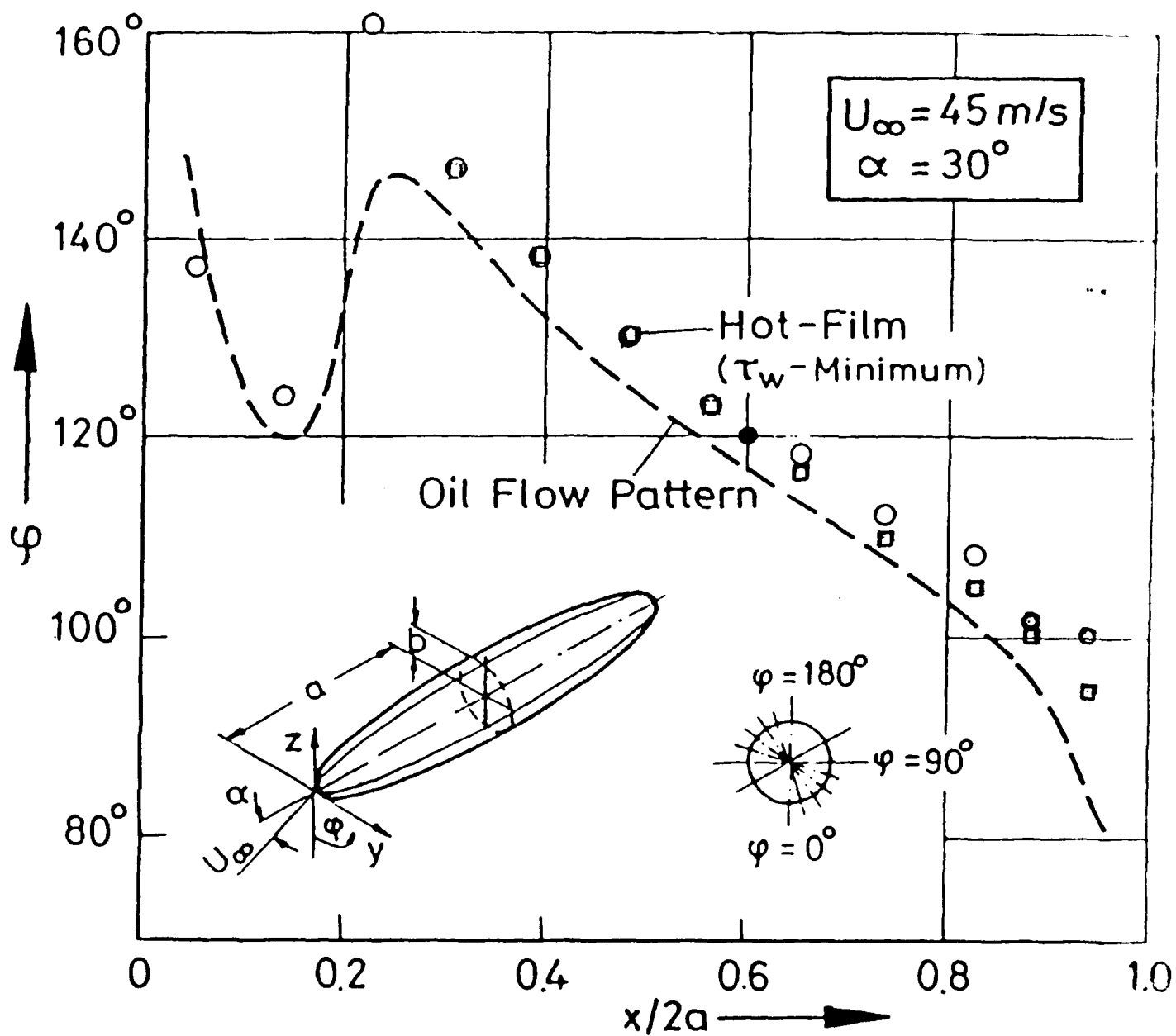Figure A.1  Wall shear stress vectors on the prolate spheroid at $\alpha = 30°$ (Kreplin et al., 1982).

Figure A.2    Comparison of separation regions obtained from oil flow patterns and surface hot film measurements, $\alpha = 30°$ (Meier and Kreplin, 1980). Circles denote location of local minimum in skin friction magnitude. Squares denote separation locations calculated by equation (A.10) and the method shown schematically in Figure A.3.
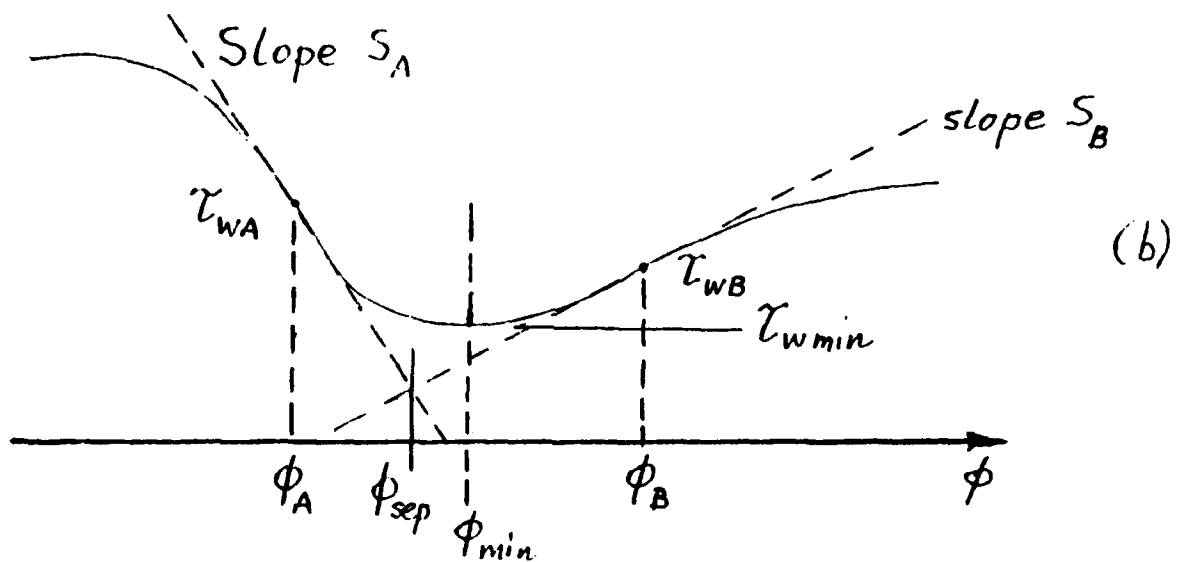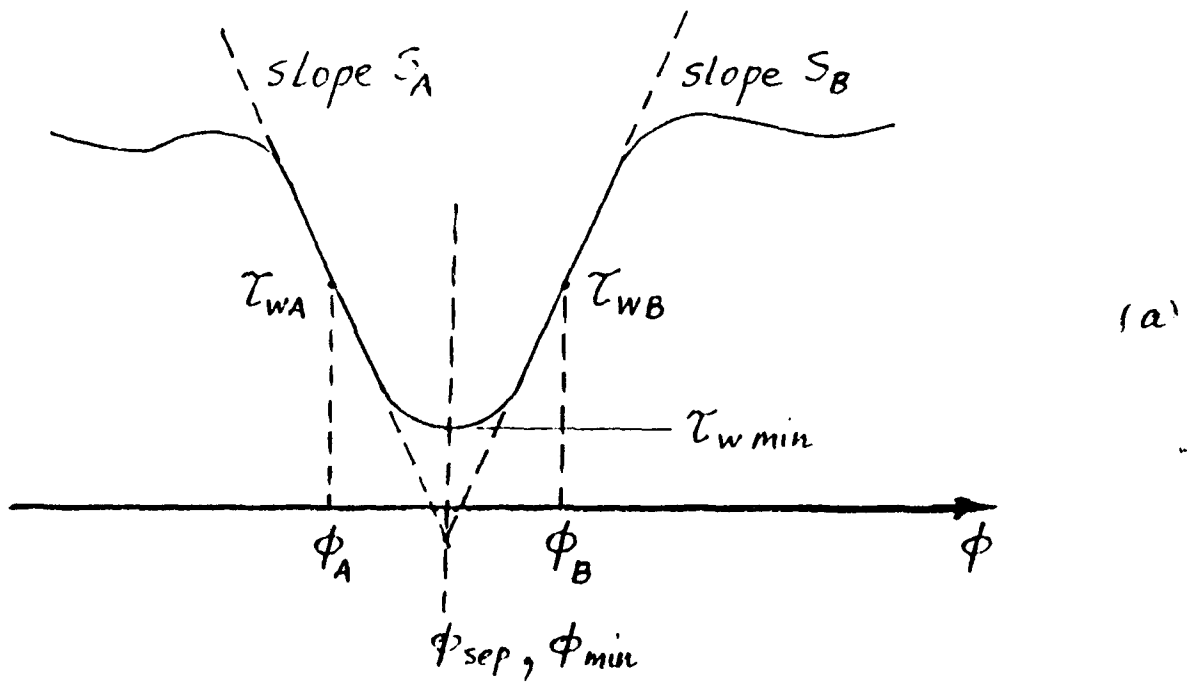
Figure A.3  Examples of variations of the wall shear stress magnitude in the vicinity of a local minimum:

(a) example of locally symmetric distribution of $|\tau_W|$ around a shear stress minimum.

(b) example of locally asymmetric distribution of $|\tau_W|$ around a shear stress minimum.